Does the Moon possess a molten core? Probing the deep lunar interior using results from LLR and Lunar Prospector

A. Khan, K. Mosegaard, J. G. Williams, P. Lognonné

Does the Moon possess a molten core? Probing the deep lunar interior using results from LLR and Lunar Prospector

A. Khan,[1] K. Mosegaard,[2] J. G. Williams,[3] and P. Lognonné[1]

Received 13 May 2004; revised 29 June 2004; accepted 12 July 2004; published 22 September 2004.

[1] It is the main purpose of this study to examine the deeper structure of the Moon in the light of four numbers. These are lunar mass M, mean moment of inertia I, second degree tidal Love number k_2, and the quality factor Q, accounting for tidal dissipation within the solid body of the Moon. The former two have been measured by Lunar Prospector to high precision, and more than 30 years of lunar laser ranging (LLR) data have led to an estimate of the second degree tidal Love number and quality factor. The inverse problem dealt with here of obtaining information on the lunar density and S wave velocity profile from the four numbers follows our earlier investigations by employing an inverse Monte Carlo sampling method. We present a novel way of analyzing the outcome using the Bayes factor. The advantage lies in the fact that rather than just looking at a subset of sampled models, we investigate all the information sampled in different runs, i.e., take into account all samples, in order to estimate their relative plausibility. The most likely outcome of our study, based on the data, their uncertainties, and prior information, is a central core with a most probable S wave velocity close to 0 km/s, density of $\sim$7.2 g/cm^3 and radius of about 350 km. This is interpreted as implying the presence of a molten or partially molten Fe core, in line with evidence presented earlier using LLR regarding the dissipation within the Moon. *INDEX TERMS:* 6250 Planetology: Solar System Objects: Moon (1221); 5430 Planetology: Solid Surface Planets: Interiors (8147); 5455 Planetology: Solid Surface Planets: Origin and evolution; 3260 Mathematical Geophysics: Inverse theory; 3210 Mathematical Geophysics: Modeling; *KEYWORDS:* mathematical geophysics, Moon, planetology, solid surface

Citation: Khan, A., K. Mosegaard, J. G. Williams, and P. Lognonné (2004), Does the Moon possess a molten core? Probing the deep lunar interior using results from LLR and Lunar Prospector, *J. Geophys. Res.*, *109*, E09007, doi:10.1029/2004JE002294.

1. Introduction

[2] The internal structure and composition of a planet or satellite are important constraints on theories for how such bodies formed and evolved. Hitherto, constraints on the interior of the Moon have been set using various geophysical methods, with the seismic data providing most of the information. Specifically, arrival time inversions resulted in information down to a depth of roughly 1100 km [e.g., *Goins et al.*, 1981; *Nakamura*, 1983; *Khan and Mosegaard*, 2002; *Lognonné et al.*, 2003], whereas a study of the lunar free oscillations provided possible constraints on the lower parts as well [*Khan and Mosegaard*, 2001], leaving the vexing question of the existence of a lunar core, in analogy with the terrestrial core, unanswered (for a review of planetary seismology, see, e.g., *Lognonné and Mosser* [1993]). The unambiguous detection of the lunar core, which so far has eluded investigators, is of prime importance as it holds the potential of distinguishing between the various theories for the formation of the Moon (for a review of these, see, e.g., *Wood* [1986]). The theory which currently enjoys the greatest success is the giant impact model, which has the Moon forming about 4.5 Gyr ago [*Halliday et al.*, 2000] from the debris produced when a Mars-sized proto-planet collided with the proto-Earth [e.g., *Cameron*, 2000; *Canup and Asphaug*, 2001]. Simulations reveal that the material from which the Moon is made up contains very little iron and consequently a lunar core, if it exists, should be small.

[3] The lunar laser ranging (LLR) experiment originally came about as a consequence of wanting to use the solar system as a testbed for gravitational theories, in particular the verification of the gravitational constant G as being independent of time. R. H. Dicke proposed LLR in the late 1950'ies as a possible means to distinguish between differing metric theories of gravity [*Will*, 1993]. Einstein's theory of gravity predicts no change in the Newtonian gravitational constant G with time, whereas a fundamental tenet of scalar tensor theories of gravity such as the one invented by *Brans and Dicke* [1961] is a time variable G.

[4] The Apollo 11 mission was the first to deploy a retroreflector on the lunar surface, consisting of corner-cube

[1]Département de Géophysique Spatiale et Planétaire, Institut de Physique du Globe de Paris, Saint Maur des Fossés, France.
[2]Department of Geophysics, Niels Bohr Institute, University of Copenhagen, Copenhagen, Denmark.
[3]Jet Propulsion Laboratory, California Institute of Technology, Pasadena, California, USA.

0148-0227/04/2004JE002294

reflectors. These reflectors have the special property of reflecting light back in the direction from which it came. Further reflectors were carried on the Apollo 14 and 15 missions as well as on two Soviet Lunokhod's of which only one was operational (for a recent historical review of the experiment and results, see *Dickey et al.* [1994]). Ranging has been done from several observatories around the world, mainly in the US and France. Laser ranging consists basically of measuring to high accuracy the distance between the lunar reflectors and the Earth observatories, through the round-trip travel time of the laser pulse. Any changes in the distance will thus manifest itself as a change in this travel time. Accuracy in the early days was measured in meters, but is now down to less than 2 centimeters. The changes in the distance are due to the orbit, the finite size of the Earth and Moon, and the time-varying rotation of the Earth and Moon.

[5] LLR data contain a wealth of information and their analysis has over the years provided improved knowledge on the dynamics and the structure of the Moon, through very accurate determination of the second- and third-degree gravitational harmonics, the moments of inertia and their differences as well as the lunar tidal Love number which all depend on the lunar internal mass distribution, composition and dynamics. The time-varying elastic tidal distortions of the Moon are detected most strongly through their influence on the rotation and orientation and more weakly on the displacements of the reflectors.

[6] Lunar Prospector which was launched in January 1998 mapped the Moon from a circular and polar orbit, 100 km above its surface, providing global maps of composition in addition to its gravity and magnetic field. The surface distribution of a number of key elements, such as H, U, Th, K, O, Si, Mg, Fe, Ti, Al and Ca, which together make up more than 98% of the mass of lunar material, provides information on the mineralogy and bulk composition of the crust and hence the origin and evolution of the Moon. The abundance of these elements was obtained using a gamma-ray and a neutron spectrometer [e.g., *Lawrence et al.*, 1998; *Feldman et al.*, 1998]. Of most importance for the present study is the improved lunar moment of inertia value obtained from the mission which provides information on the interior density distribution [*Konopliv et al.*, 1998].

[7] It is the main purpose of the present paper to infer information about the deep interior of the Moon, not least to try to substantiate the existence of a liquid core, by inverting several geophysical observations obtained through LLR analysis and Doppler tracking of the Lunar Prospector spacecraft, specifically, the second degree tidal Love number, mass, moment of inertia and the tidal quality factor. It is envisioned that the data investigated here will be able to provide information on the deeper parts of the lunar interior where the seismic data were less sensitive.

[8] This kind of investigation is of great interest, not only from an inverse problem theoretical point of view, but also from a planetary aspect, since the data considered here can be obtained from the tracking of orbiting spacecraft, thereby furnishing us with a means of obtaining information to first order on the deeper interiors of planets, something which is usually not possible without seismic data. The effects of core size and state on the tidal Love number have been calculated most recently for Mercury in anticipation of the upcoming Messenger and BepiColombo missions [e.g., *Spohn et al.*, 2001; *Van Hoolst and Jacobs*, 2003], for Mars [*Yoder et al.*, 2003; *Van Hoolst et al.*, 2003] as well as for the satellites of the giant planets [e.g., *Anderson et al.*, 2001; *Castillo et al.*, 2002; *Sohl et al.*, 2003].

[9] As regards the inversion, the framework needed to formalize the inverse problem involves the use of probability density functions (*pdf*'s) to represent every single state of information in the problem [*Tarantola and Valette*, 1982; *Tarantola*, 1987]. The outcome, given by the posterior *pdf*, is obtained by combining all available information. Samples from this posterior *pdf* are then obtained by employing a Markov Chain Monte Carlo method (MCMC) [e.g., *Mosegaard and Tarantola*, 1995]. As in the study of *Khan and Mosegaard* [2002], the posterior results will be analyzed using Bayesian hypothesis testing. However, we will present a variant of this scheme which employs, as something new, all information sampled, rather than being limited to the information carried in a subset of the sampled model space.

2. Theory

[10] This section presents the basic theory of the deformation of a spherically symmetric self-gravitating planet and how this is related to the Love numbers. As the subject matter is treated extensively in the literature we shall just present the equations concerning the elastic case and refer the reader to, e.g., *Dahlen* [1972] for the general case, i.e., that of a rotating, self-gravitating, slightly perturbed planet at an applied frequency ω.

[11] The global deformations that a planet experiences include among others those due to tides and rotation, which can be represented by harmonic potentials. Let us for the present purposes consider a harmonic gravitational potential (not necessarily a homogeneous one) of degree n and frequency ω acting on an elastic sphere and being due to the gravitational attraction of the Earth:

$$V = \sum_n V_n(r) S_n e^{i\omega t} \tag{1}$$

with S_n being a surface spherical harmonic. The basic problem now rests in determining the deformation of the planet subject to this potential, using the equations of motion for a self-gravitating elastic body [e.g., *Bullen*, 1963]:

$$\rho \frac{\partial^2 \mathbf{u}}{\partial t^2} = (\lambda + \mu)\nabla(\nabla \cdot \mathbf{u}) + \mu \nabla^2 \mathbf{u} + \rho \nabla V + \rho \mathbf{g}, \tag{2}$$

where $\mathbf{u} = (u_r, u_\theta, u_\phi)$ is the displacement vector in spherical coordinates, ρ the density, $\mathbf{g}$ the gravity, λ is related to μ and κ (shear and bulk modulus) through $\lambda = \kappa - 2\mu/3$. We also have to consider the additional potential arising from the redistribution of mass which must satisfy Poisson's equation within the planet. It is implicitly assumed that all parameters involved in equation (2) are functions of radius. These equations are of course to be solved using appropriate boundary conditions, which include regularity of the solution at the origin, vanishing of the stresses on the deformed surface of the planet and continuity of potentials and their gradients across boundaries. An analogy can be

drawn to the theory of free oscillations of a planet, since in this case we are also concerned with deformations, although at a different frequency and thus the only thing which distinguishes the two cases is essentially the tidal forcing frequency. A convenient method of reducing the above equations to six linear differential equations in the Runge-Kutta form has been introduced by *Alterman et al.* [1959] in a study of the oscillations of the Earth and can be summarized as

$$\frac{dy_i^n}{dr} = \Omega_{;ij}\,(\lambda(r), \mu(r), \rho(r), g(r), n, \omega) y_j^n i, \quad j = 1, \ldots, 6, \qquad (3)$$

where the y_i's correspond to harmonic deformations of degree n and are, respectively, the radial factors of the radial displacement (y_1), the radial stress (y_2), the tangential displacement (y_3), the tangential stress (y_4), the potential perturbation (y_5) and perturbation in potential gradient (y_6) and finally the Ω_{ij}'s are functions of the rheological parameters, the harmonic degree and frequency of the deformation. The six first-order differential equations can then be solved numerically using the appropriate boundary conditions. Having set the stage we can now present the general solution for the displacement which takes the form [e.g., *Lambeck*, 1988]

$$\mathbf{u}(r) = \sum_n \left[y_1^n(r) S_n \mathbf{e_r} + y_3^n(r) \nabla S_n \mathbf{e_t} \right] e^{i\omega t}, \qquad (4)$$

where $\mathbf{e_r}$ and $\mathbf{e_t}$ are unit vectors in the radial and tangential direction, respectively. In much the same way that the displacement in the theory of free oscillations in general is made up of a sum of a spheroidal and a torsional part, this is also the case here. Since the spheroidal part of the displacement also involves physical deformation of the figure of the body, whereas this is not the case in the torsional part, there is associated with it an additional potential, V', arising from this redistribution of mass:

$$V' = \sum_n y_5^n(r) S_n e^{i\omega t}. \qquad (5)$$

In 1909 Love obtained the deformation at the surface of the Earth ($r = a$) due to an applied potential, given in the form of equation (1) [e.g., *Melchior*, 1978] as

$$\mathbf{u_n}(a) = \frac{1}{g}(h_n(a) S_n \mathbf{e_r} + l_n(a) \nabla S_n \mathbf{e_t}) V_n'(a) e^{i\omega t}, \qquad (6)$$

where g is the value of gravity at the surface ($r = a$). The extra potential was written as

$$V'(a) = \sum_n k_n(a) V_n S_n e^{i\omega t}, \qquad (7)$$

introducing the three Love numbers, h_n, l_n, k_n, of degree n. From a comparison of (4) and (5) with Love's derivations, (6) and (7), we immediately see that

$$h_n(a) = y_1^n(a), \quad l_n(a) = y_3^n(a), \quad k_n(a) = y_5^n(a).$$

From this it is clear that the Love numbers are dependent upon the structural parameters of the planet and thus once we have a specific model of a planet we can calculate the Love numbers using the solutions (4) and (5). Having said this, it is clear that analytical solutions for the Love numbers exist only for very simple models. One of these which considers the Earth to be an incompressible homogeneous elastic sphere, also known as the Kelvin Earth model, for which the Love numbers can be shown to be given by the following relations [e.g., *Lambeck*, 1988]:

$$h_n = \frac{2n+1}{2(n-1)(1+\bar{\mu})}, \quad l_n = \frac{3}{2n(n-1)(1+\bar{\mu})}, \quad k_n = \frac{3}{2(n-1)(1+\bar{\mu})}, \qquad (8)$$

where

$$\bar{\mu} = \frac{\mu \Xi_n}{\rho g a} = \frac{v_s^2 \Xi_n}{g a}, \quad \Xi_n = \frac{2n^2 + 4n + 3}{n}, \qquad (9)$$

and v_s is the seismic shear wave velocity. Now, while this model is clearly an oversimplification and is shown here only for purposes of illustration, it is still employed to provide approximate results for planetary bodies on whose interior structure we know little or nothing about. In addition, equations (8) and (9) have the property of clearly emphasizing the dependence of the Love numbers on the structural parameters, μ and ρ. More generally, it has to be noted that k_n also depends on the bulk modulus, albeit to a much lesser extent than the shear modulus, through the dependency of the y_i's on the Lamé parameter, λ, as is seen from equation (3).

[12] Dissipation of energy associated with the anelasticity of a planet is usually expressed in terms of the quality factor Q. The elastic parameters above become frequency-dependent and complex when damping is taken into account. As for the elastic case we shall briefly outline the theory underlying the viscoelastic situation (for details the reader is referred to, e.g., *Zschau* [1978], *Wahr and Bergen* [1986], and *Segatz et al.* [1988]). In the following we shall express the global dissipation as a function of parameters that depend on the internal structure of the planet.

[13] The average global dissipation over one orbit can be obtained by using the following relation for the rate at which energy is dissipated in the planet's interior:

$$\frac{dE}{dt} = \int_\Omega \left[\rho \frac{\partial \mathbf{u}}{\partial t} \cdot \nabla W \right] d\Omega + \int_\Sigma \left[\frac{\partial \mathbf{u}}{\partial t} \cdot \mathbf{T} \right] d\Sigma, \qquad (10)$$

where the square brackets denote the average over one orbital period, $\mathbf{u}$ is the displacement vector, ρ the density in the unperturbed state, $\mathbf{T}$ the surface traction and W is the total tidal potential, given by the sum of the external tide raising potential V and the additional potential V' due to the mass redistribution within the planet and symbols Ω and Σ denote integration over volume and surface, respectively. The first integral represents the rate at which work is done by body forces and the second that done by surface tractions.

[14] Starting with equation (10) and employing Green's first integral transformation to transform the volume integral into a surface integral, it is possible to directly express the

global dissipation as a function of the Love number k_2 (limiting ourselves to the tidal potential of degree 2) and the tidal potential integrated at the surface ($r = a$) of the planet [*Zschau*, 1978; *Segatz et al.*, 1988]

$$\frac{dE}{dt} = -\frac{5\omega}{8\pi^2 Ga}\int_{\Sigma}\left[V'\frac{\partial V}{\partial t}\right]d\Sigma, \tag{11}$$

where G is the gravitational constant and a the planetary radius. For a purely elastic body the time integral would vanish as the external tide raising potential is in phase with the potential arising from the redistribution of mass within the planet. For a dissipating satellite, however, the phase angle between the two potentials becomes nonzero and so does the integral in equation (11). Introducing the second order complex Love number $k_2 = Re(k_2) + iIm(k_2)$ and using the proportionality between the two potentials V and V', equation (7), as well as the fact that $Im(k_2)/Re(k_2) \ll 1$ is generally valid for planetary interiors, we can write equation (11) as [*Segatz et al.*, 1988]

$$\frac{dE}{dt} = -\frac{5Im(k_2)}{8\pi^2 Ga}\int_{\Sigma}\left[\frac{\partial V}{\partial t}\right]^2 d\Sigma. \tag{12}$$

Upon inserting an expression for the tide raising potential [e.g., *Goldreich*, 1967] into the above relation and additionally using equation (7), we obtain the global tidal dissipation rate due to the body tide for a synchronous body in an inclined and eccentric orbit with obliquity α (where the obliquity is measured from orbit plane to the lunar equator), eccentricity e and orbital period $2\pi/\omega$

$$\frac{dE}{dt} = -\frac{(\omega a)^5}{G}Im(k_2)\left[\frac{21}{2}e^2 + \frac{3}{2}\sin^2(\alpha)\right]. \tag{13}$$

Given that the global dissipation factor Q^{-1} is defined as the ratio of the energy ΔE dissipated during an orbit to the peak energy stored in the system during the same cycle, Q^{-1} can also be expressed in terms of the Love number, namely as the ratio between its imaginary part and its modulus

$$Q^{-1} = Im(k_2)/|k_2| \simeq Im(k_2)/Re(k_2). \tag{14}$$

As $Re(k_2)$ and $Im(k_2)$ depend on the interior structure of the planet, so will Q.

3. Analysis: Inversion of k_2, M, I, and Q

3.1. Statement and Solution of the Inverse Problem

[15] The problem has been stated loosely in the introduction and will be reiterated more rigorously here. The problem consists of inferring information on the interior structure of the Moon through four numbers obtained from the analysis of LLR and the tracking of Lunar Prospector and earlier spacecraft, specifically, the second degree tidal Love number, k_2, the mean moment of inertia I, mass M and the tidal quality factor Q. The measured values are $M = 7.3477 \pm 0.003310^{22}$ kg and $I/MR^2 = 0.3935 \pm 0.0002$ (M. A. Wieczorek et al., manuscript in preparation, 2004), based on the value of *Konopliv et al.* [1998] and rescaled to a mean radius R of 1737.1 km [*Smith et al.*, 1997]. The LLR determined value of $k_2 = 0.0227 \pm 0.0025$ and monthly $Q = 33 \pm 4$ [*Williams et al.*, 2004].

[16] To solve the inverse problem posed here a Markov Chain Monte Carlo (MCMC) method will be used. Only a short presentation of the methodics underlying the MCMC algorithm will be discussed here, since the details are amply reviewed elsewhere [e.g., *Mosegaard and Tarantola*, 1995; *Mosegaard*, 1998; *Kaipio et al.*, 2000; *Mosegaard and Sambridge*, 2002; *Khan and Mosegaard*, 2002].

[17] In the most general case we have an equation of the form

$$\mathbf{d} = \mathrm{g}(\mathbf{m}), \tag{15}$$

where g contains the physical laws relating a given model, $\mathbf{m}$, to data, $\mathbf{d}$. Given the fact that we are in possession of data and are interested in estimating what sort of model is implied by these, our problem could thus be stated as the inverse of equation (15), that is, $\mathbf{m} = \mathrm{g}^{-1}\mathbf{d}$. However, as simple as this might seem, in practice it is somewhat more difficult, since g^{-1} does not generally exist. Moreover, the functional g is usually not available as an analytical expression for the forward relation between data and model parameters, but can be replaced by an algorithm allowing data to be calculated for any given model.

[18] Within the Bayesian framework the inverse problem is viewed as a problem of combining several states of information using probability densities, describing everything from prior information on model parameters, $\eta(\mathbf{m})$, over what is known from the direct measurement of observable parameters to the information contained in the physical laws relating model and data, $L(\mathbf{m})$. The likelihood function is usually of the form, $L(\mathbf{m}) = k\exp(-S(\mathbf{m}))$, where k is a normalization constant and $S(\mathbf{m})$ is known as the misfit function and is a measure of how well data calculated using $\mathbf{m}$ fit the observed data. It should be noted that the likelihood function presented here actually constitutes several parts, since the present problem is concerned with different types of geophysical information. In this case the likelihood function can be written as the product of a number of likelihood functions pertaining to the individual data if it is assumed that the observational uncertainties and calculation errors are independent among the different geophysical methods employed, that is,

$$L(\mathbf{m}) = \prod_{\alpha} L_{\alpha}(\mathbf{m}), \tag{16}$$

where $L_{\alpha}(\mathbf{m})$ is the likelihood function for every independent geophysical method [*Bosch*, 1999].

[19] The solution, then, to our inverse problem is given by the combination of these states of information into another state, which is known as the posterior probability density function (*pdf*):

$$\sigma(\mathbf{m}) = k\eta(\mathbf{m})L(\mathbf{m}), \tag{17}$$

where k is a normalization constant [*Tarantola and Valette*, 1982; *Tarantola*, 1987; *Mosegaard and Tarantola*, 1995]. The main idea is therefore to design a random walk in the model space which samples the posterior probability density, i.e., samples models that are consistent with data

and prior information. Markov chain sampling methods are usually the ones invoked, because of their ergodic properties in sampling *pdf*'s. It is said that a Markov chain is ergodic to a *pdf* if any set of model outcomes from a sampling run converges to a sample from the particular *pdf*, that we wish to sample, as the number of steps increases [*Tierney*, 1994; *Kaipio et al.*, 2000; *Mosegaard and Sambridge*, 2002]. One of the methods most commonly used to achieve this is the Metropolis algorithm or importance sampling algorithm which works according to the following rules [e.g., *Mosegaard*, 1998]:

[20] 1. In iteration $i + 1$ propose a new model $\mathbf{m}_{\text{new}}^{i+1}$ around the neighborhood of the current model $\mathbf{m}_{\text{current}}^{i}$ by running one step of the random walk that samples the prior η_i.

[21] 2. Accept $\mathbf{m}_{\text{new}}^{i+1}$ with probability

$$P_{accept} = \min\left(1, \frac{L_{new}}{L_{current}}\right)$$

[22] 3. If $\mathbf{m}_{\text{new}}^{i+1}$ is accepted then $\mathbf{m}_{\text{current}}^{i+1} = \mathbf{m}_{\text{new}}^{i+1}$ otherwise $\mathbf{m}_{\text{current}}^{i+1} = \mathbf{m}_{\text{current}}^{i}$ and steps 1 to 3 are repeated.

[23] A factor of great importance, especially when we are concerned with high-dimensional spaces, where a large proportion of the volume may have near-zero probability density, is that this algorithm renders us capable of sampling the space with a sampling density proportional to the given probability density without excessively sampling low-probability areas of the space.

3.2. Analysis: The Bayes Factor as an Estimator

[24] $\sigma(\mathbf{m})$ presents the solution to our inverse problem and let us now go on to analyze this distribution in some detail. A typical approach in a Bayesian analysis of $\sigma(\mathbf{m})$ would be to conjure up questions concerning the physical nature of the interior of the body under investigation which are evaluated using resolution measures of the form [e.g., *Mosegaard*, 1998]

$$\mathcal{R}(\Lambda, f) = \int_{\Lambda} f(\mathbf{m})\sigma(\mathbf{m})d\mathbf{m}, \tag{18}$$

where $f(\mathbf{m})$ is a given function of the model parameters $\mathbf{m}$ and Λ is an event or subset of the model space containing the models of current interest. However, for the general inverse problem the posterior *pdf* does not exist as an analytical function and given its usually complex shape defined over a high-dimensional model space it can not be integrated analytically. Instead we have to estimate posterior probabilities by statistical integration methods which consist of approximating the integral above by a summation over a large number of models, $\mathbf{m}_1, \ldots, \mathbf{m}_N$, sampled according to $\sigma(\mathbf{m})$, whereby the resolution measure can be written as

$$\mathcal{R}(\Lambda, f) \approx \frac{1}{N} \sum_{\{n|\mathbf{m}_n \in \Lambda\}} f(\mathbf{m}_n). \tag{19}$$

[25] As there are no well-posed nor ill-posed questions within the Bayesian paradigm, only questions which have a probabilistic answer, a query concerning the lunar core could be formulated as follows:

[26] • On the basis of the observed data, their uncertainties and prior information, what is the most probable state of the lunar core?

[27] The approach taken here is very much in line with that adopted by *Khan and Mosegaard* [2002] where the Bayesian scheme was extended to compare any two hypotheses, i.e., questions, corresponding to different parts of the model space, directly against each other, rather than simply evaluating resolution measures. The advantage in computing Bayes factor for testing the relative plausibility of any two hypotheses over the calculation of single resolution measures was made obvious. Bayesian hypothesis testing will also be our present main approach of analysis. However, we will take the analysis one step further, in that we will take advantage of all the information contained in the posterior distribution as opposed to that contained in only a limited number of samples.

[28] Let $f(\mathbf{x})$ to be an unnormalized probability distribution and let us consider the problem of evaluating

$$\mathcal{F} = \|f\| \equiv \int_{\mathcal{M}} dV(\mathbf{x}) f(\mathbf{x}). \tag{20}$$

Now, if $\{\mathbf{x}_1, \mathbf{x}_2, \ldots, \mathbf{x}_k\}$ is a sample of $f(\mathbf{x})$ in the model space $\mathcal{M}$ containing k points, let us furthermore consider the expression

$$J_k = \frac{1}{V\,k} \sum_{i=1}^{k} \frac{1}{f(\mathbf{x}_i)}, \tag{21}$$

where V is the volume sampled. This expression is generally applicable to any distribution which has been sampled using an importance algorithm. Clearly, J_k is well-defined, as no samples will be collected at points $\mathbf{x}_i$ where $f(\mathbf{x}_i) = 0$. The expectation of J_k is

$$\begin{aligned} E(J_k) &= \frac{1}{V\,k} \sum_{i=1}^{k} E\left(\frac{1}{f(\mathbf{x}_i)}\right) \\ &= \frac{1}{V\,k}\, k\, E\left(\frac{1}{f(\mathbf{x})}\right) \\ &= \frac{1}{V} \frac{\int_{\mathcal{M}} dV(\mathbf{x})}{\int_{\mathcal{M}} dV(\mathbf{x}) f(\mathbf{x})} \\ &= \frac{1}{\mathcal{F}}. \end{aligned} \tag{22}$$

[29] In other words, J_k is an unbiased estimator of $1/\mathcal{F}$ and should $f(\mathbf{x})$ happen to be normalized, then $E(J_k) = 1$ (K. Mosegaard and A. Tarantola, manuscript in preparation, 2004).

[30] This sets the stage for the following example, whose purpose is to relate the probability distribution $f(\mathbf{x})$ through equation (21) to the Bayes factor (usually alluded to Turing [see *Good*, 1988]), which is used in Bayesian hypothesis testing.

[31] **Definition (Bayes Factor)** Given two hypotheses $\mathcal{H}_i$ and $\mathcal{H}_j$ corresponding to assumptions of alternative classes of models, M_i and M_j, for data $\mathbf{d}$, with prior probabilities $q(M_i)$ and $q(M_j)$ and posterior probabilities $p(M_i)$ and $p(M_j)$,

the Bayes factor in favor of $\mathcal{H}_i$ (and against $\mathcal{H}_j$) is given by the posterior to prior odds ratio

$$B_{ij}(\mathbf{d}) = \left(\frac{p(M_i)}{p(M_j)}\right) \Big/ \left(\frac{q(M_i)}{q(M_j)}\right). \tag{23}$$

Consider now the special case where the prior probability distribution over the model space is a uniform probability distribution of the form $\rho(\mathbf{m}) = 1/V$, where V is the volume of the entire model space. In this case we have

$$\frac{q(M_i)}{q(M_j)} = \frac{V_i}{V_j}. \tag{24}$$

The posterior probabilities of the two classes of models are estimated as integrals

$$p(M_i) = \int_{M_i} \sigma(\mathbf{m}) d\mathbf{m} = C \int_{M_i} L(\mathbf{m}) d\mathbf{m} \tag{25}$$

and

$$p(M_j) = \int_{M_j} \sigma(\mathbf{m}) d\mathbf{m} = C \int_{M_j} L(\mathbf{m}) d\mathbf{m}, \tag{26}$$

where C is a constant, and $L(\mathbf{m}) = \sigma(\mathbf{m})/\rho(\mathbf{m}) = V\,\sigma(\mathbf{m})$ is the likelihood function. We now have

$$B_{ij}(\mathbf{d}) = \left(\frac{L(M_i)}{L(M_j)}\right) \Big/ \left(\frac{V_i}{V_j}\right), \tag{27}$$

where

$$L(M_i) = \int_{M_i} L(\mathbf{m}) d\mathbf{m} \tag{28}$$

and

$$L(M_j) = \int_{M_j} L(\mathbf{m}) d\mathbf{m} \tag{29}$$

are integrated likelihoods over M_i and M_j, respectively. It follows now from equation (23) that if $\{\mathbf{m}_1, \mathbf{m}_2, \ldots, \mathbf{m}_k\}$ is a sample from M_i of L $(\mathbf{m})$ containing k points, and $\{\hat{\mathbf{m}}_1, \hat{\mathbf{m}}_2, \ldots, \hat{\mathbf{m}}_\ell\}$ is a sample from M_j of L $(\mathbf{m})$ containing ℓ points, then

$$S_i^{(k)} = \frac{1}{k} \sum_{r=1}^{k} \frac{1}{L(\mathbf{m}_r)} \tag{30}$$

and

$$S_j^{(\ell)} = \frac{1}{\ell} \sum_{s=1}^{\ell} \frac{1}{L(\hat{\mathbf{m}}_s)} \tag{31}$$

are estimators of $V_i/L(M_i)$ and $V_j/L(M_j)$, respectively, enabling us to write

$$B_{\ell k} = \frac{S_j^{(\ell)}}{S_i^{(k)}} \tag{32}$$

as an estimator of $B_{ij}(\mathbf{d})$. Consequently, the interpretation of the Bayes factor is such that if $B_{\ell k} > 1$, $\mathcal{H}_i$ is relatively more plausible given $\mathbf{d}$; if, on the other hand, $B_{\ell k} < 1$, then $\mathcal{H}_j$ has increased in relative plausibility. The interpretation of the Bayes factor as put forward here is thus seen to be the same as the one given by *Khan and Mosegaard* [2002]. So what is the difference? The approach taken by *Khan and Mosegaard* [2002] was to sample the model space given data and general prior information resulting in a diverse set of models. Once the model space had been sampled sufficiently to provide us with an adequate coverage of models highlighting diverse characteristics was Bayesian hypothesis testing implemented, by searching for those models that were contained in the respective areas of the model space as dictated by whatever hypotheses we were currently interested in. The present approach is thus clearly seen to be a variant of this in that we fix from the outset the different areas of the model space that we want to sample, as outlined by the respective hypotheses, corresponding to assumptions of alternative classes of models of interest and then use all sampled models, rather than a subset as done previously, to evaluate the Bayes factor. It is thus clear that the advantage with the present method lies in the fact that we are taking all samples into account. On a more technical note it just means running separate algorithms corresponding to the different hypotheses of current interest and then using all the samples from these runs to evaluate the Bayes factor as given in equation (32). Any number of hypotheses or runs can thus be analyzed by this method and compared.

3.3. Forward Problem

[32] The forward problem consists of calculating data, in this case Love number, moment of inertia, mass and dissipation, given a set of model parameters, i.e., a model of the subsurface structure of the Moon. The program that calculates the second degree tidal Love number uses as entry a subsurface model of the density (ρ), P (v_p) and S wave (v_s) velocity. The present model of the Moon is divided into 5 spherically symmetric concentric shells of variable size. The 5 shells correspond to crust, upper mantle, middle mantle, lower mantle and core, respectively, in line with the divisions inferred from seismic data [e.g., *Nakamura*, 1983; *Khan et al.*, 2000; *Khan and Mosegaard*, 2001]. To each shell is attached one parameter characterizing its physical extent, three material parameters in the form of the density, ρ, shear and bulk moduli, μ and κ, respectively. Given the elastic moduli the wave velocities are easily calculated from the usual expressions:

$$v_p = \sqrt{\frac{\kappa + 4\mu/3}{\rho}}, \qquad v_s = \sqrt{\frac{\mu}{\rho}}, \tag{33}$$

whereas M and I only depend upon the density structure and are evaluated using the following expressions:

$$I = \frac{8\pi}{3}\int \rho(r) r^4 dr, \qquad M = 4\pi \int \rho(r) r^2 dr. \tag{34}$$

To calculate the tidal dissipation within the moon, or equivalently, the inelastic contribution to k_2 we shall employ the following scheme. As already noted the elastic parameters become complex and frequency-dependent when inelasticity is taken into account. If Q is independent of frequency then μ is given by [*Wahr and Bergen*, 1986] (as done by *Zschau* [1978], we assume that there are only losses of mechanical energy in shear and none in pure compression)

$$\mu = \mu_0 \left[1 + \frac{1}{Q}\left(\frac{2}{\pi}\ln\left(\frac{\omega}{\omega_0}\right) + i\right)\right], \tag{35}$$

where μ_0 is the value of μ at the reference frequency ω_0 and all values refer to global properties, i.e., the homogeneous case. If we make the additional assumption that μ is also independent of ω, then μ reduces to

$$\mu = \mu_0 + i\frac{\mu_0}{Q}. \tag{36}$$

From this expression we see that the effect of Q is to perturb μ only slightly and thus that the imaginary part of μ, i.e., μ_0/Q, which is a measure of the dissipation, contributes very little. So, in order to calculate the imaginary part of μ, we define a local quality factor, q, which measures the amount of energy being dissipated within each shell and the ratio, μ_0/q, in every shell thus makes up the imaginary contribution to μ as a function of depth. Thus, to calculate the dissipation or equivalently the imaginary part of k_2, we shall use the following scheme. We employ the set of parameters $\{r_j, \rho_j, \mu_j, \kappa_j\}$ to calculate the purely elastic part of k_2 and label it k_2'. Having done this, let us perturb μ in layer j from μ_j to $\mu_j + \delta\mu_j$, where $\delta\mu_j = \mu_j/q_j$ and $\delta\mu_j \ll \mu_j$. Using this new value for μ_j, let us recompute the Love number and designate it k_2''. From this we can estimate the derivative of the Love number with respect to μ in layer j as $dk/d\mu = (k_2'' - k_2')/\delta\mu$. Then to first order in $1/Q$, the value of the Love number for an inelastic Moon will be

$$k_2 = k_2' + i\sum_{j=1}^{5}\frac{dk_j}{d\mu_j}\delta\mu_j = k_2' + i\delta k_2. \tag{37}$$

Comparing this with the expression for k_2 in the general case, i.e., $k_2 = Re(k_2) + iIm(k_2)$, we see that δk_2 makes up the imaginary contribution to the Love number. Having thus estimated its inelastic part, we can use equation (14) to determine the global dissipation.

3.4. Inverse Problem

3.4.1. Prior Sampling of Models

[33] In the previous section the parameters delineating our model of the Moon were presented. They included the position of layer boundaries, r_i, the density ρ_i, the elastic moduli μ_i and κ_i as well as the local quality factor, q_i, with $i = 1, \ldots, 5$. As already noted in the previous section the forward algorithm calculating the tidal Love number uses as input a model of the density, P and S wave velocity structure. The reason we chose the elastic moduli as parameters to describe our system instead of ρ, v_s and v_p is because the former parameters constitute the most natural description of our system, since the wave velocities are only an indirect manifestation of the material parameters through the relations (34). As a further refinement we shall take another step in parameterizing our system, by adopting, not simply ρ, μ, κ and q, but rather their logarithms, $\log(\rho/\rho_0)$, $\log(\mu/\mu_0)$, $\log(\kappa/\kappa_0)$ and $\log(q/q_0)$ as parameters and assume that they are homogeneously distributed, with ρ_0, μ_0, κ_0 and q_0 being arbitrary constants (here $\rho_0 = 1$ kg/m^3, $\mu_0 = 1$ Pa, $\kappa_0 = 1$ Pa and $q_0 = 1$). Let us denote the logarithmic parameters as ρ', μ', κ' and q'. The reason for this choice is that the homogeneous probability distribution for the positive parameters themselves, ρ, μ and κ, takes the form $\mathcal{F}_{\rho\mu\kappa} = 1/\rho\mu\kappa$ which remains invariant for any power of ρ, μ, and κ [*Mosegaard and Tarantola*, 2002]. Thus our physical system, that is, our model of the Moon, is now represented by the following model parameter vector $\mathbf{m} = \{r_i, \rho_i', \mu_i', \kappa_i', q_i'\}$ which consists of 25 parameters in all.

[34] Let us start out by explaining how the algorithm, in using a set of random rules whose efficiency has been optimized through a number of numerical experiments, samples prior information. In every iteration all parameters are changed. First a shell is selected uniformly at random and so are the values of the parameters to be changed. The physical extent of a given shell, d_i, defined by the radii of the layer boundaries, r_i and r_{i+1}, can take on any value within certain confines. As noted, our model parameterization follows the major delineations as inferred from the seismic studies and these are used as guidelines in perturbing the thickness of a given layer. Boundaries are set according to the results of *Khan and Mosegaard* [2002]. These boundaries are then allowed to take on any value within the confines of the boundaries ultimately above and below the boundary under consideration, while the radius of the lunar surface and center are anchored at $r = 1737$ km and $r = 0$ km, respectively. Concerning the density and the elastic moduli, ρ, μ and κ, their logarithms are assumed to be homogeneously distributed within some interval which is given by the probability density:

$$\eta(\mathbf{m}) = \exp\left(-\sum_i \frac{\left(m_i - m_{prior}\right)^p}{p\sigma^p}\right), \tag{38}$$

where m_i are the components of any one of the parameters to be sampled, that is, ρ', μ' or κ'. m_{prior} and σ are appropriately chosen logarithmic average values and deviations, respectively and p is the order (here $p = 30$; $\mu_{prior}/\mu_0 = 19$; $\sigma_\mu = 5.5$; $\kappa_{prior}/\kappa_0 = 19.5$; $\sigma_\kappa = 5.5$; $\rho_{prior}/\rho_0 = 8.5$; $\sigma_\rho = 0.5$). Prior information in the form of equation (38) has been chosen because it makes an adequate approximation to a simple homogeneous probability distribution defined in some interval. The local quality factors, q', are homogeneously distributed in the interval [0;5]. Generating samples from this distribution in the model space is mathematically given by $m_i^{new} = m_i' + \xi(2\alpha - 1)$, where ξ

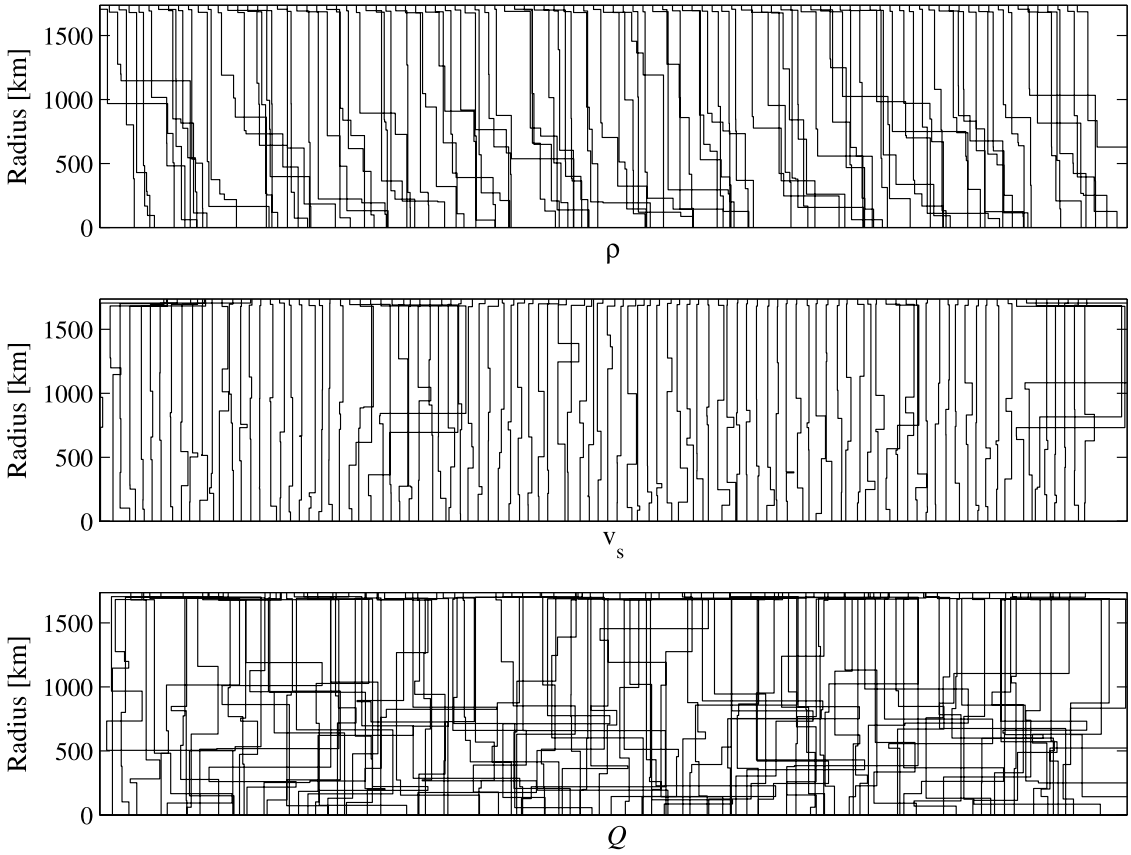

Figure 1. One hundred samples taken from the prior probability distribution satisfying $\mathcal{H}_1$ and showing, from top to bottom, ρ, v_s, and Q as a function of radius. The horizontal separation between individual corresponds to 0.5 g/cm^3 (ρ), 0.3 km/s (v_s), and 10 (Q). Note that as we are not plotting the logarithm of the individual parameters, we do not obtain homogeneous distributions, but ones that are skewed. The models plotted here all contain liquid low-velocity cores ($v_s \leq 0.5$ km/s) as prescribed by $\mathcal{H}_1$.

is a constant controlling the length of the steps that are taken in the model space, typically of the order of 1, α is a uniformly distributed number in the interval [0;1] and primes signify logarithms. Given the slightly different approach taken here in analyzing the posterior distribution entailing the sampling of different parts of the model space corresponding to various classes of models of current interest, i.e., hypotheses, let us briefly enumerate these. As we are mostly concerned with the presence and state of the lunar core, we will limit ourselves to exploring the model space occupied by the following prior information (presented as hypotheses, corresponding to the assumption of two alternative classes of models M_1 and M_2):

Hypothesis 1 ($\mathcal{H}_1$): The lunar core is molten.

Hypothesis 2 ($\mathcal{H}_2$): The lunar core is solid.

As the parameter which determines the physical state in each layer i is the shear modulus μ and the innermost shell ($i = 1$) is taken as representing the core we can also write for the above two hypotheses, $\mathcal{H}_1$: $\mu'_1 \in$ [0;20] and $\mathcal{H}_2$: $\mu'_1 \in$ [24;28]. This means that all parameters pertaining to the central shell are left variable as just described, apart from the shear modulus which is also variable, but confined to the indicated intervals. These two models for the core are obviously end-member models and more complicated structures could in principle also be considered.

[35] As no relation between the elastic parameters has been assumed here, we have made the additional assumption that models with a $\rho \geq 4.5$ g/cm^3 correspond to either solid or liquid material. What this means is that if the density in a layer other than the innermost, in a given iteration, is perturbed and attains a value $\geq$4.5 g/cm^3, then in the same iteration, it is randomly decided (with equal probability) whether μ is perturbed within the liquid or solid range (in conformity with the above two hypotheses). The reason why this prior constraint has been adopted was to avoid sampling layers with a combination of intermediate velocities and densities lying in the heavy end of the spectrum, which are more difficult to interpret. It should be noted that in case the density in that same layer is <4.5 g/cm^3, then none of the just mentioned restrictions apply to μ, meaning that it can assume values in conformity with equation (38).

[36] Concerning perturbation of the density, the scheme just described still holds, although slightly modified, in order to sample density structures in a more sensible way. It is clear that if we were to blindly perturb the density in

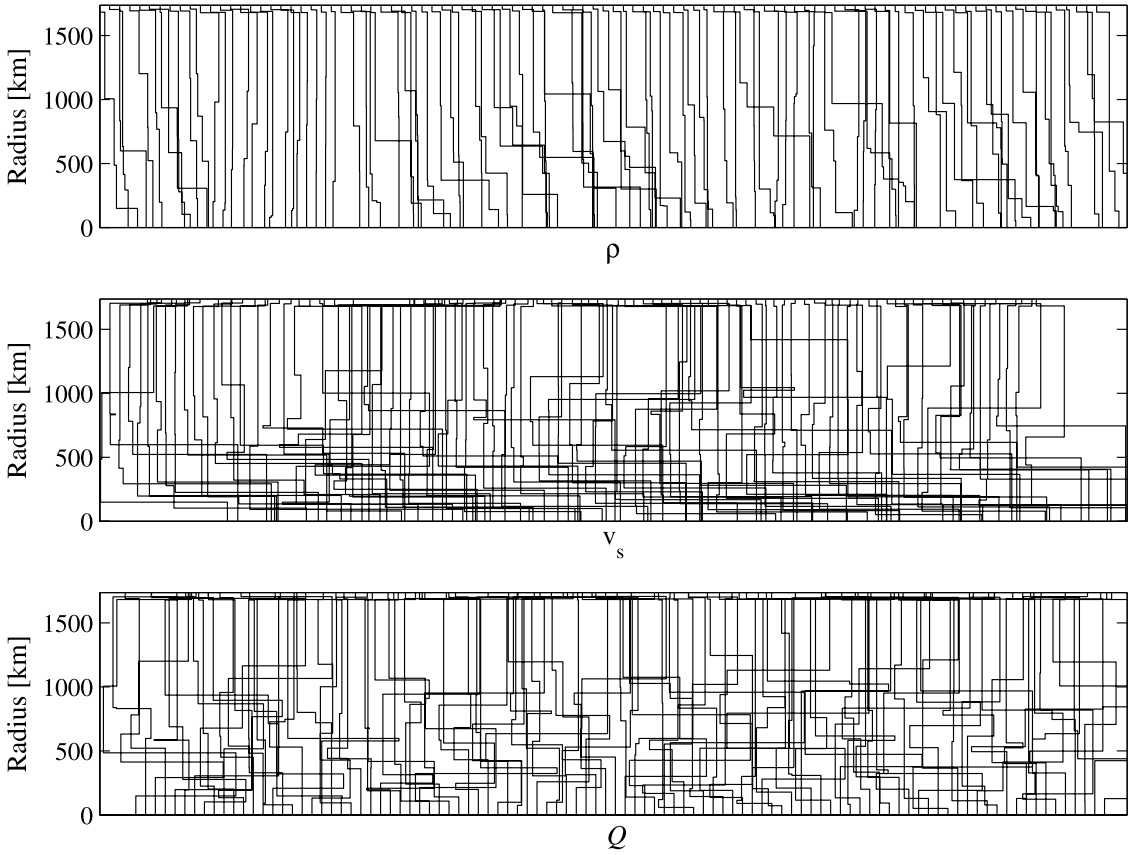

Figure 2. One hundred samples taken from the prior probability distribution satisfying $\mathcal{H}_2$ and showing, from top to bottom, ρ, v_s, and Q as a function of radius. The horizontal separation between individual corresponds to 0.5 g/cm^3 (ρ), 0.3 km/s (v_s), and 10 (Q). Note that as we are not plotting the logarithm of the individual parameter, we do not obtain homogeneous distributions, but ones that are skewed. The models plotted here are all contain solid cores ($v_s \geq 3.5$ km/s) as prescribed by $\mathcal{H}_2$.

any given layer by some arbitrary large amount the resulting total mass and moment of inertia for this new density model might change drastically leading to almost certain rejection of the model. The modification added in sampling densities alluded to above concerns therefore the step length. Let us label the perturbation of the density in layer i, $\Delta\rho_i$, whose size is subject to a number of conditions, which are as follows. The total change in mass is minimized by offsetting the addition of mass in layer i by the subtraction of an equal amount of mass in the layer below and vice versa if mass is subtracted in layer i. The same scheme holds true in case of the moment of inertia. The final $\Delta\rho_i$ is then obtained by taking an average among the density changes, minimizing on the one hand, change in total mass, and on the other, change in total moment of inertia. The second condition that the density perturbation has to satisfy stems from the fact that only density models that increase with depth are of interest. Thus the final density change has to satisfy the sequence $\ldots\ \rho_{i+2} \leq \rho_{i+1} \leq \rho_i \leq \rho_{i-1} \leq \rho_{i-2}\ \ldots$ Let us finally note that an upper bound on the crustal density has been set at 3 g/cm^3, in general agreement with measurements on lunar crustal samples [*Taylor*, 1982], while for the core the upper bound is 7.5 g/cm^3.

[37] This body of information, then, serves as prior knowledge, in the sense that the algorithm samples the model space with a probability density describing exactly this information. Figure 1 shows prior information regarding the parameters v_s, ρ, and Q for a number of samples satisfying $\mathcal{H}_1$, while Figure 2 depicts prior information for the same parameters in accordance with $\mathcal{H}_2$.

3.4.2. Posterior Sampling of Models

[38] Having sampled prior information we are now ready to update this using data to obtain the posterior distribution. As is obvious from equation (17) data are taken into account through the likelihood function. The expression for the likelihood function is, assuming data to be individually independent and identically distributed gaussian uncertainties

$$L(\mathbf{m}) \propto \exp\left(-\frac{\left(d^I_{obs} - d^I_{cal}(\mathbf{m})\right)^2}{2\sigma_I^2} \cdot -\frac{\left(d^M_{obs} - d^M_{cal}(\mathbf{m})\right)^2}{2\sigma_M^2} - \frac{\left(d^{k_2}_{obs} - d^{k_2}_{cal}(\mathbf{m})\right)^2}{2\sigma_{k_2}^2} - \frac{\left(d^Q_{obs} - d^Q_{cal}(\mathbf{m})\right)^2}{2\sigma_Q^2} \right), \quad (39)$$

where d_{obs} denotes observed data, $d_{cal}(\mathbf{m})$ synthetic data computed using model $\mathbf{m}$ with superscripts alluding to the particular geophysical observation and σ is the uncertainty on either of these.

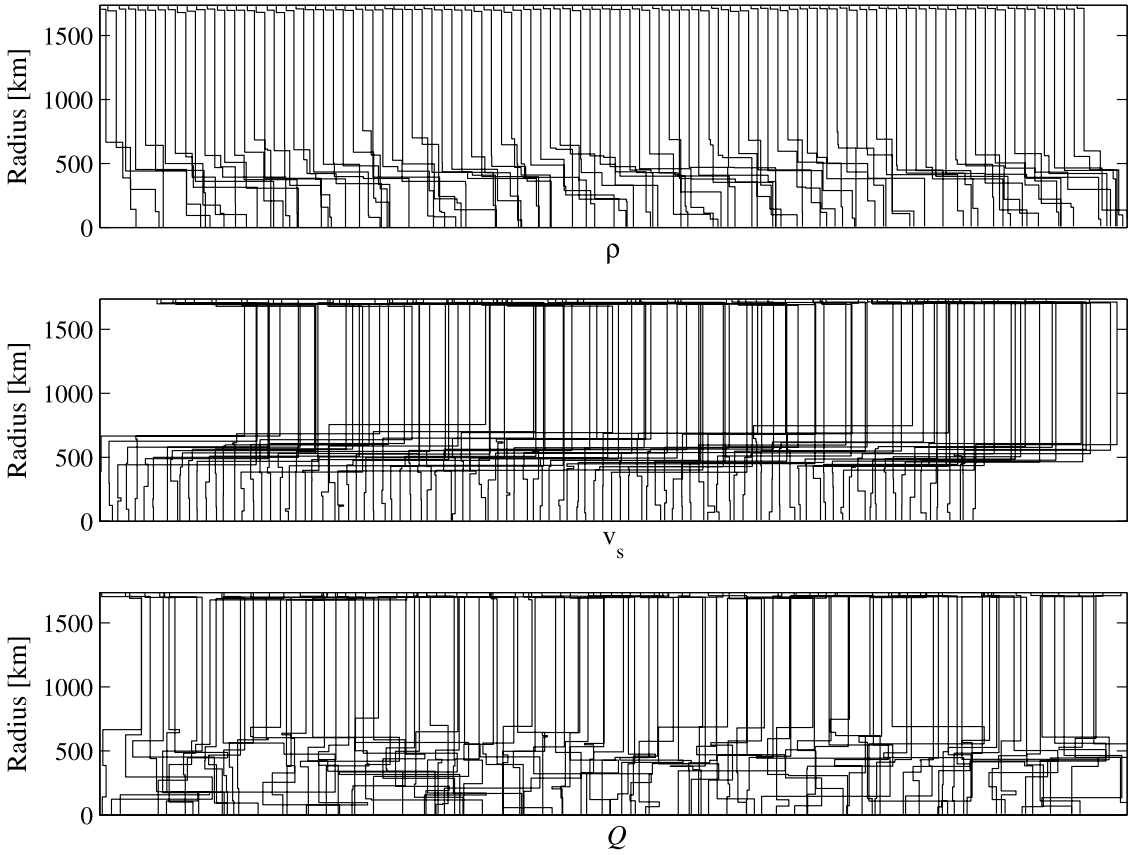

Figure 3. One hundred samples taken from the posterior probability distribution satisfying $\mathcal{H}_1$ and showing, from top to bottom, ρ, v_s, and Q as a function of radius. The horizontal separation between individual corresponds to 0.5 g/cm^3 (ρ), 0.3 km/s (v_s), and 10 (Q). As in Figure 1, we are not plotting the logarithm of the individual parameters and so do not obtain homogeneous distributions, but ones that are skewed. The models shown here are to be compared with Figure 1, and a significant narrowing is visible, highlighting features that are well-resolved.

[39] In each iteration a shell was chosen at random and subsequently all parameters pertaining to this shell were perturbed using the proposal distribution as defined in the previous section. The adopted proposal distribution has a burn-in time of the order of 1000 iterations after which the retention of samples commences. In all 5 million models have been sampled and to ensure near-independent samples every 100th model has been retained for further analysis with an overall acceptance rate of 35%. In Figures 3 and 4, a number of samples from the posterior distribution are displayed, showing v_s, ρ and Q as a function of depth for the two hypotheses. A comparison with prior information on the same parameters (Figures 1 and 2) provides us with an indication of those structures within the Moon which are well resolved as well as ill resolved.

[40] Since k_2, as already noted, mostly depends upon the shear modulus and therefore provides very little information on bulk modulus and hence P wave velocity, we will not be concerned with the latter two parameters.

4. Analysis: Estimating the Most Probable State of the Lunar Core

[41] The question that we are currently interested in could be formulated as follows (in line with the one posed before):

[42] • How likely is it, given the observed data, their uncertainties as well as prior information, that the Moon has a molten, partially molten or solid Fe, Fe-S alloy or dense silicate core (the latter may contain elevated Fe and Ti abundances and will henceforth be abbreviated ilmenite core)?

[43] In attempting to answer this question we will be using our two hypotheses: $\mathcal{H}_1$: The lunar core is molten. $\mathcal{H}_2$: The lunar core is solid. Figure 5 shows the negative logarithm of the likelihood values as a function of iteration number for the two runs that are used in evaluating the Bayes factor, which is found to be, using equation (32), $B_{12} = 0.00014$. As $B_{12} < 1$, it signifies that $\mathcal{H}_1$ is more plausible than $\mathcal{H}_2$ or in words that, given data and prior information, a liquid or partially molten core is more probable than a solid core.

5. Results

[44] A selection of prior and posterior models has already been shown in the preceding sections and here we shall be more concerned with addressing questions of resolution and uncertainty. These items which are of immense importance when having to draw conclusions from inverse calculations are frequently addressed in the form of a covariance matrix and the like (this is espe-

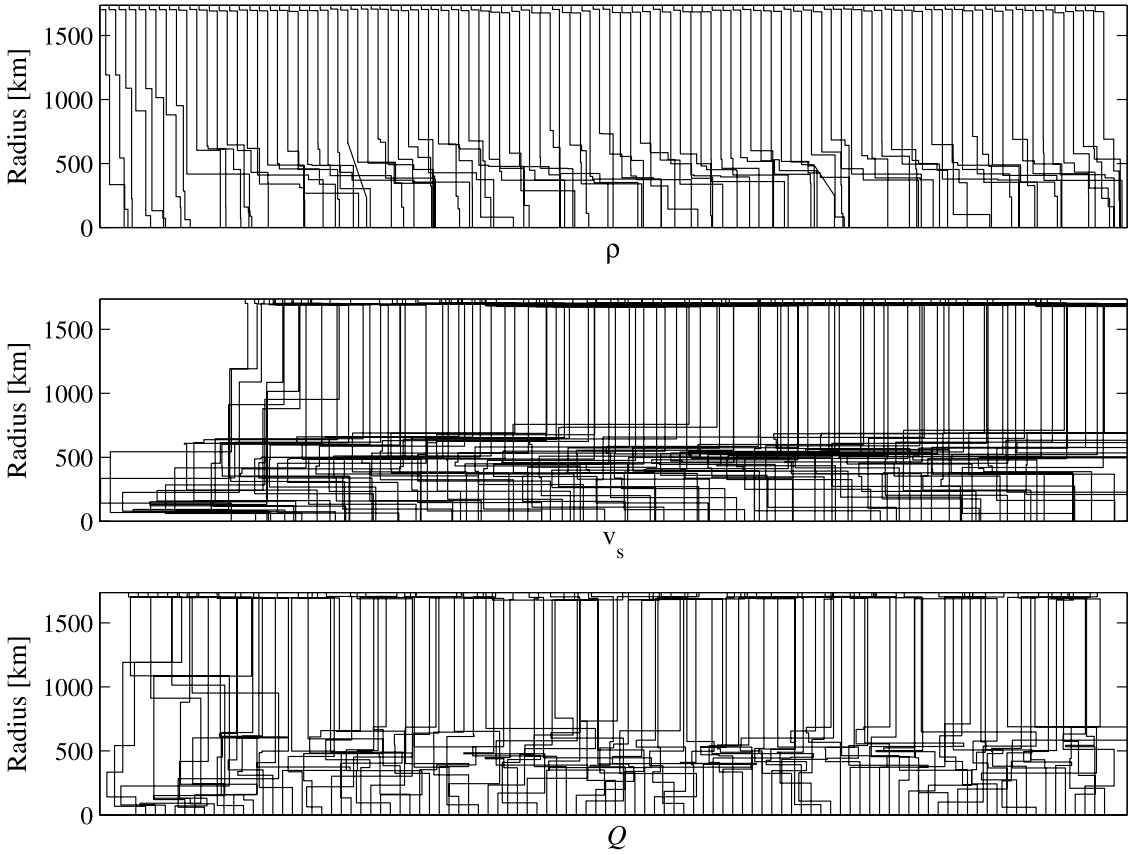

Figure 4. One hundred samples taken from the posterior probability distribution satisfying $\mathcal{H}_2$ and showing, from top to bottom, ρ, v_s, and Q as a function of radius. The horizontal separation between individual corresponds to 0.5 g/cm^3 (ρ), 0.3 km/s (v_s), and 10 (Q). As in Figure 1, we are not plotting the logarithm of the individual parameters and so do not obtain homogeneous distributions, but ones that are skewed. The models shown here are to be compared with Figure 2, and a significant narrowing is visible, highlighting features that are well-resolved.

cially true for linear inverse problems) which have become the standard tool by which these items are assessed. For the general inverse problem we consider the aforementioned matrices as inadequate and therefore resort to other ways to convey information on uncertainty and resolution. For the general inverse problem treated from the statistical point of view it is by no means a simple task to display a set of graphs that sensibly provide a clear indication of the results. A reasonably direct way to display the results would be by means of a prior and posterior movie as exemplified by *Mosegaard and Tarantola* [1995]. What has been displayed in Figures 1 to 4 is strictly taken not a movie, but could be more adequately considered as a collection of models. For the purpose of rendering the reader with a sense of the resolution contained in the results we will present figures plotting prior next to posterior models as a direct comparison reflects how much information is actually contained in the data.

[45] As the model including a liquid/partially molten core (henceforth referred to as liquid core) is found to be the most likely outcome given data and prior information, we shall now only be concerned with the samples from $\mathcal{H}_1$ and take a closer look at these in order to answer the question as to the most probable density and size of the core.

[46] As the innermost shell is taken as being representative of the core, Figure 6 displays its prior and posterior ρ and size distribution using one-dimensional (1-D) marginal posterior probability distributions (*ppd*). While these are rather intuitive and therefore easy to interpret, the information that can be extracted from them is restricted, since marginals are constructed by regarding all other parameters as nuisance parameters and integrating them out, i.e.,

$$\mathcal{P}(m_k|\mathbf{d},\mathcal{I}) = \int_0^\infty \sigma(m_k,\mathbf{m}'|\mathbf{d},\mathcal{I})d\mathbf{m}', \qquad (40)$$

where m_k is the parameter of interest, $\mathbf{d}$ is our data vector, $\mathcal{I}$ prior information and $\mathbf{m}'$ is the parameter vector containing all other parameters than m_k. A first look at the marginal *ppd* tells us, as concerns the density of the core (Figure 6c), that the greatest amount of probability is relegated to the heavy end of the spectrum, that is for values of the density around 7 g/cm^3. The marginal radial *ppd* for the core (Figure 6d) indicates core sizes in the range from 70 km to 450 km. Above ~450 km the probability is close to zero, which is in line with other estimates as to its maximum possible size (see the next section). A question which immediately poses itself is, what is the size distribution for those cores with a

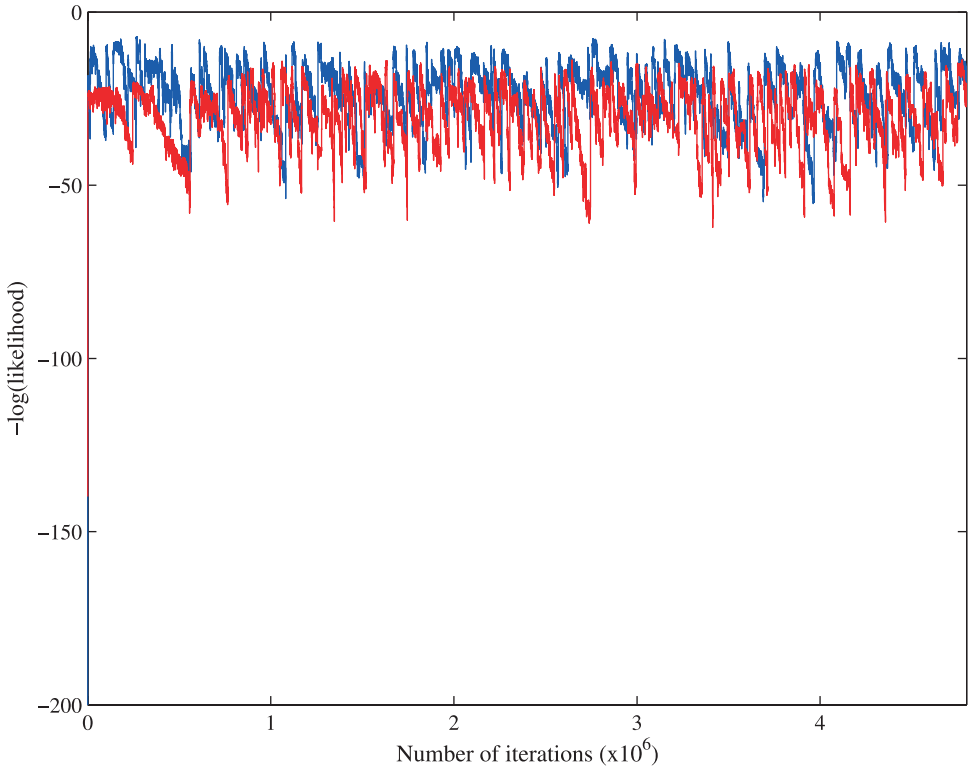

Figure 5. The negative logarithm of the likelihood functions for the runs corresponding to the two hypotheses $\mathcal{H}_1$ (blue line) and $\mathcal{H}_2$ (red line). Equation (39) defines the likelihood function quantitatively; qualitatively, we can say that the likelihood function is a measure of how well a given model fits observed data. With this definition in mind, it is clear that models including liquid cores are seen to fit data better.

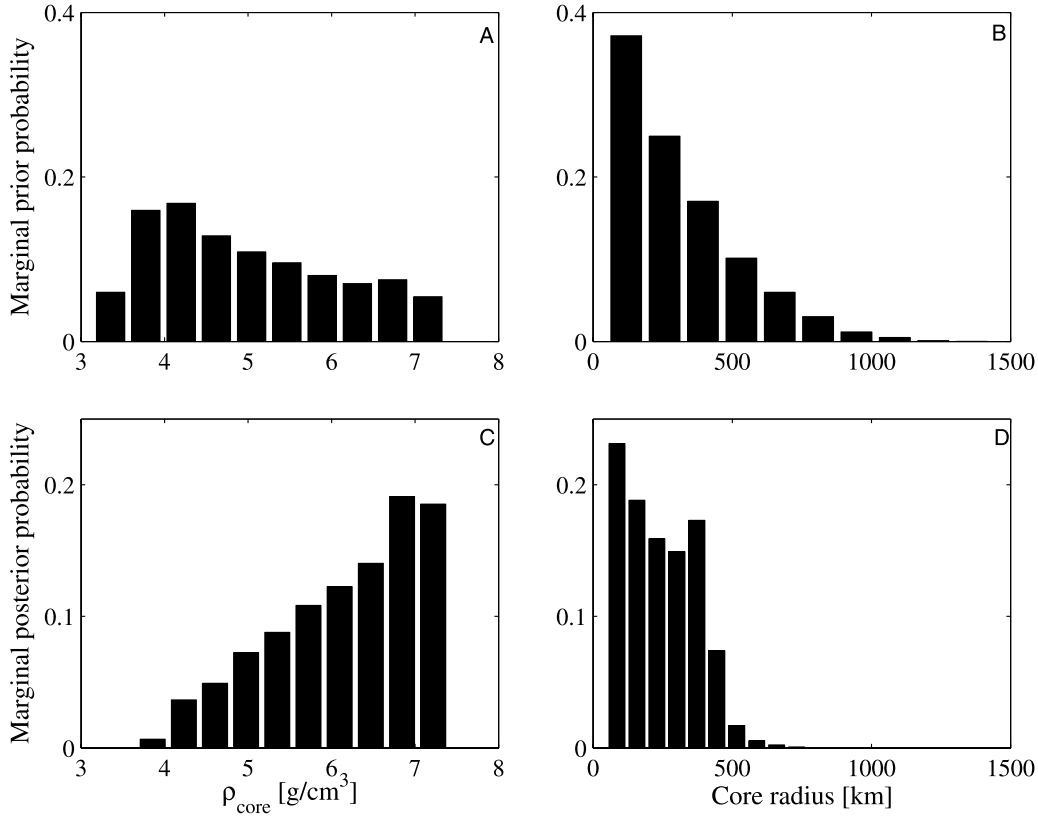

Figure 6. One-dimensional (a and b) marginal prior and (c and d) posterior histograms for sampled values of the density and radius of the core. A comparison of prior and posterior clearly shows how prior information regarding these two parameters has been changed by taking data into account.

density around 7 g/cm^3? However, as discussed above this sort of information can not be extracted from the 1-D marginal *ppd*'s as it has been integrated out. To obtain this information involves investigating the correlation between the two parameters of interest, here ρ and core radius, which is displayed below for all five layers contained in our model of the Moon, as 2-D prior (Figure 7) and posterior (Figure 8) *pd*'s. From these figures it can be seen that there exists a high probability for a core with a radius of around 350 km and density ∼7.2 g/cm^3. Other possibilities are of course also possible, most notably there seems to be a large probability for a core with a density of ∼6 g/cm^3 and radius around 400 km, although it has to be noted that the peak is much narrower and not as high as the other one. A certain care should be exercised in interpreting very localized extrema, such as the latter peak, since it might not necessarily contain the highest probability integrated over a given interval. This would be the case if the peak turns out to be very narrow. It will, in spite of its prominent amplitude, only contain a small fraction of the total probability as its integrated probability (the total area beneath it) is very small.

[47] The 2-D *pd*'s displayed here are actually conditional probability distributions and therefore differ from the marginal distribution, $\mathcal{P}(m_k|\mathbf{d}, \mathcal{I})$ above (disregarding the fact that one is 2-D and the other 1-D). In general, while they both describe our inference about the given parameter of interest they correspond to different circumstances, in that the marginal *pd* takes into account prior ignorance of all the other parameters $\mathbf{m}'$, whereas a conditional probability density employs any information available about any other parameter m_i, i.e.,

$$\mathcal{P}(m_k|\mathbf{d}, m_i, \mathcal{I}) = \int_0^\infty \sigma(m_k, \overline{\mathbf{m}}|\mathbf{d}, m_i, \mathcal{I}) d\overline{\mathbf{m}}, \qquad (41)$$

where $\bar{\mathbf{m}}$ is a parameter vector containing all parameters other than m_k and m_i. Depending on the circumstances this can lead to a significant narrowing of the *ppd*. The difference between equations (40) and (41) is illustrated in Figure 9, where we have plotted the 1-D marginal *ppd* for sampled core densities as well as the conditional *ppd* for those cores that are *conditioned* on having radii in the range 300 km $\leq r \leq$ 400 km.

[48] In much the same way that we investigated the correlation between the central density and its radius we can go on and take a look at the relationship between the *S* wave velocity of the core and its radius. This is plotted below as prior and posterior 2-D marginal *pd*'s in Figures 10 and 11 from which the most probable core velocity and size can be inferred. From the *ppd* for the core a notable spike is apparent at about r = 350 km and v_s very close to zero which is not contained in the prior. This agrees very well with the inferences made from Figure 8 as to the most probable core radius.

[49] Finally, let us study the correlation between the parameters ρ and v_s for the core. Figures 12 and 13 depict prior and posterior 2-D marginal *pd*'s for the correlation between these two parameters. It is obvious how prior information has been amended by data and posterior indicates with a high probability a core with $\rho \sim 7.2$ g/cm^3 and v_s close to zero as consistently inferred hitherto.

[50] At this point one might be interested in asking the very pertinent question as to how much information concerning the density of the core is actually provided by the Love number. Despite the well determined nature of lunar mass and moment of inertia, the density and size of the core is not well constrained as there exists a trade-off between exactly these two parameters. So, in order to gain insight into the sensitivity of the Love number to core density, state and size, we undertook a similar inversion to the one investigated here, but without including as data k_2 and Q, that is, we inverted only mass and moment of inertia. Figure 14 displays the 1-D marginal *ppd* for all samples of core density and size distribution (compare with Figure 6) and Figure 15 shows, in the same way as Figure 8 above, the correlation between ρ and thickness of the individual layers, while Figure 16 contains a collection of samples from the posterior distribution showing v_s, ρ and Q as a function of radius (compare with Figures 1 and 3). Comparing these figures leaves little doubt that there are significant differences present and thus that k_2 and Q are indeed sensitive to the deep lunar structure, with most of the information concerning v_s coming from the Love number. Figures 1 and 3 show that the dissipation factor is mostly sensitive to mantle structure.

[51] In much the same way described above we can infer information about the mantle and crust, including its most probable shear wave velocity, density and dissipation structure. The crust is generally less well constrained, except for its density structure, where tight constraints are imposed by the moment of inertia. However, as the mantle and crust are not the main objective of this study, they will not be discussed further.

6. Discussion and Conclusion

[52] Having presented the posterior results, we are now ready to discuss these in the light of the chosen model, the inversion and any further assumptions made.

[53] Concerning our model of the Moon the assumption of spherical symmetry was made and the models obtained are thus to be viewed as angular averages over the entire Moon. As regards the inversion we face the usual trade-off between resolution and uncertainty. The resolution adopted here was found on the grounds that the distribution of calculated data provided an adequate fit to the observed data distribution. Finally, the assumption has also been made that the elastic moduli are mutually independent. This assumption is justifiable given that we are not considering any specific chemical composition for which there obviously exists a definite relation between the elastic moduli governing their behavior as a function of pressure and temperature. As regards our assumption of equation (36) that Q and the elastic moduli are independent of frequency, *Williams et al.* [2004] have shown that Q as a function of tidal period can be expressed in terms of a power-law as $33(\text{Period}/27.212\text{days})^{0.05}$. In numbers this means that Q increases from 33 at a month to 38 at one year, signaling a slight but for our purposes negligible increase. Concerning the inverse problem we have obviously taken the most general approach in solving it. The advantage of the probabilistic approach lies in its inherent ability to fully incorporate nonlinearities into the final solution, obviating any form of linearization of the original problem, providing more realistic error limits to the results for a given resolution. However, it should always be kept in mind that the final results are conditioned on the validity of the assumptions made. As regards the inversion conducted here one might argue that since we are introducing prior constraints so as to sample certain regions of the model space, the outcome which is effectively controlled by the hypotheses and consisting of two end-member scenarios (either an entirely fluid or solid core), should not come as a surprise. While this to a certain degree is true, it should be remembered that the decision process itself, by which we mean the act of having to distinguish between two hypotheses given data and prior information, is governed by Bayes theorem. Bayes theorem can be regarded as the process by which we learn and this is at the heart of our treatment of the general inverse problem, whose solution is formulated in the most general manner as the conjunction of the various states of information as emulated by Bayes theorem [*Tarantola and Valette*, 1982]. With this in mind it should be clear that the probabilities which we have calculated here are mathematical entities that are based on the quantitative information which has been used as input in the inversion. Stated differently, the probabilities that we calculate are based entirely on (1) data and their uncertainties, (2) prior information as quantified here, and (3) the physical relation between data and unknown model parameters. *Jaynes* [1985], a strong proponent of the Bayesian paradigm, has stated this succinctly by saying "...we consider the class of all hypotheses ($\mathcal{H}_1 \ldots \mathcal{H}_n$) consistent with the one data set d_{obs} that was actually observed. In addition we use prior information $\mathcal{I}$ that represents our knowledge (from physical law) of the possible ways in which nature could have generated the various $\mathcal{H}_i$. Out of the class of hypotheses consistent with our data, we pick the one favoured by the prior information $\mathcal{I}$."

[54] Before carrying on with the main discussion, we would like to draw the attention of the reader to an interesting aspect of the obtained mantle structure. From a comparison of Figures 1, 3, and 16, it is obvious that the shear wave velocity profile is essentially constrained by k_2 and Q. While it would have been straightforward to add the results obtained on the shear wave velocity structure from the arrival time inversion as prior information in this study, we chose not to do so, on the grounds that we wanted to include as few prior constraints as possible, in order to learn how much information is actually contained in the data. It is therefore very interesting and in a certain sense also reassuring to note that in the present inversion the range of probable shear wave velocities in the upper mantle are in rough agreement with the results from the arrival time inversions [e.g., *Goins et al.*, 1981; *Nakamura*, 1983; *Khan et al.*, 2000; *Lognonné et al.*, 2003].

[55] From the analysis presented here, where the hypothesis regarding a liquid state of the lunar core was found to

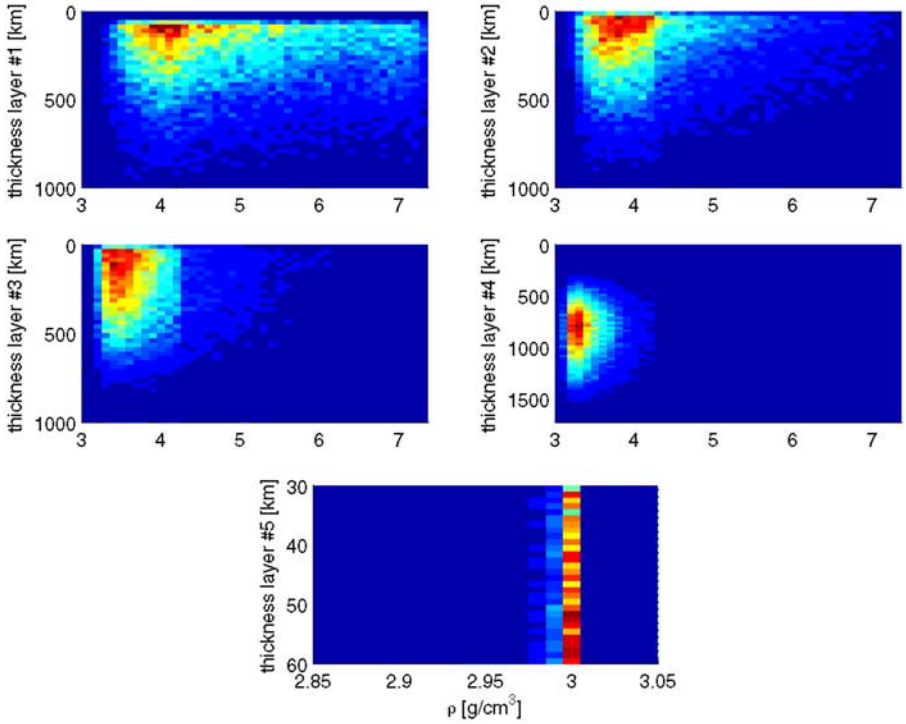

Figure 7. Two-dimensional conditional prior probability density depicting the correlation between parameters ρ and *d* (thickness) for each individual layer. Layer #1 corresponds to the core, and layer #5 corresponds to the crust. Colors indicate probability, with dark red signifying the most probable solution and dark blue signifying the least probable solution.

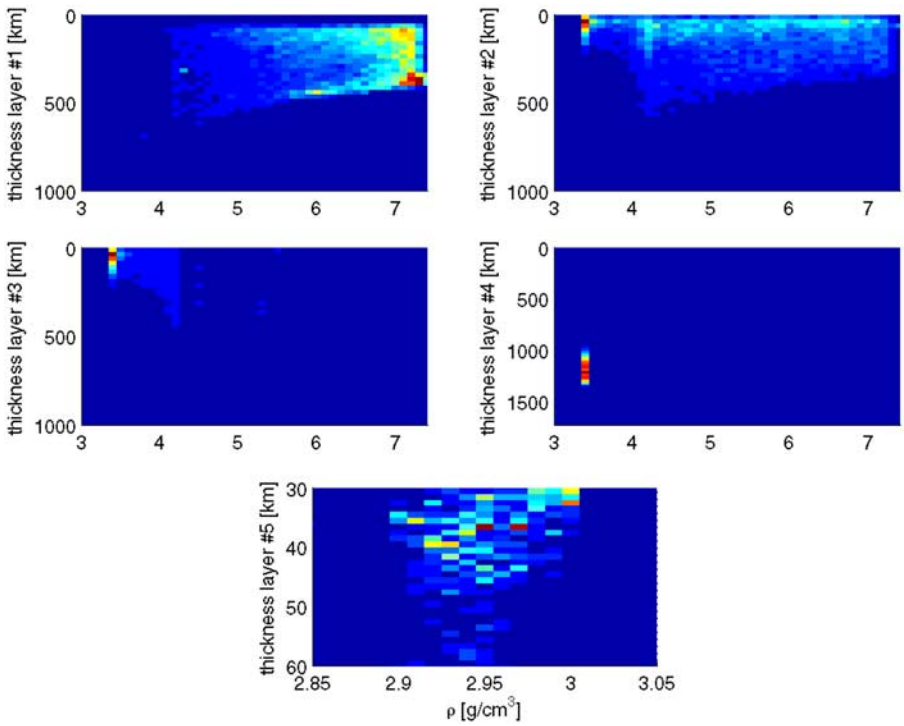

Figure 8. Two-dimensional conditional posterior probability density showing, as in Figure 7, the correlation between ρ and *d* (thickness) for each individual layer. Layer #1 corresponds to the core, and layer #5 corresponds to the crust. Color coding as in Figure 7. Comparison with prior information (Figure 7) shows a significant change of the distribution concerning the core, due to data, with a large amount of probability centered at $r \sim 350$ km and $\rho \sim 7.2$ g/cm^3. Another possibility, although less probable, is also apparent at $r \sim 400$ km and $\rho \sim 6$ g/cm^3.

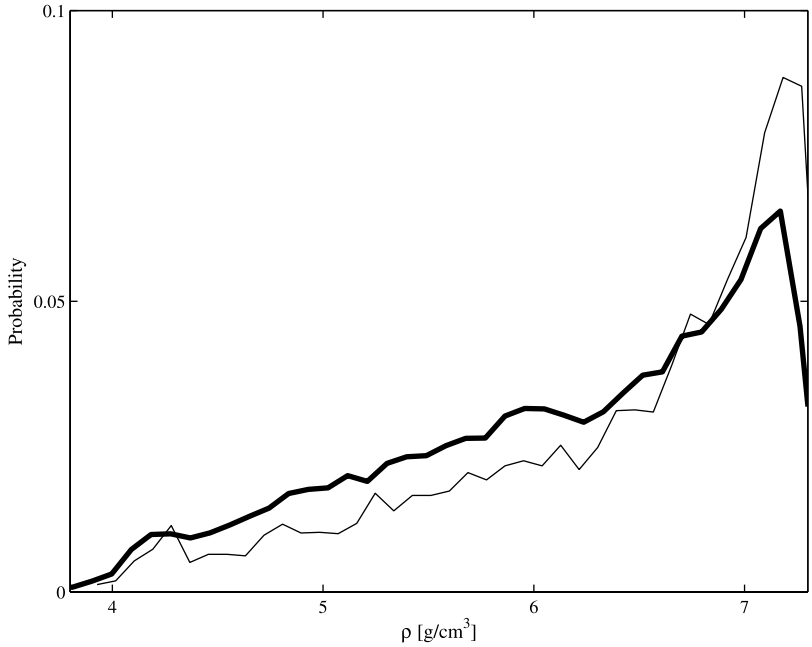

Figure 9. One-dimensional marginal posterior probability distribution (thick line) and 1-D conditional posterior probability distribution (thin line) for sampled core densities, highlighting their differences and the narrowing that has occurred for the conditional distribution as more information is considered (see main text for further clarification).

be the most likely, as the Bayes factor $B_{12} < 1$, the existence of a molten or partially molten core must be regarded as the most plausible scenario. This is in accordance with the results obtained by *Williams et al.* [2001] (hereafter referred to as Williams et al.), where a liquid core was inferred from an analysis of more than 30 years of LLR data, through the detection of a displacement of the Moon's pole of rotation indicating that dissipation is acting on the rotation. As sources of the dissipation Williams et al. argued for two effects, one being due to monthly solid-body tides raised by the Earth and Sun and the other as stemming from a fluid core, with a rotation distinct from that of the solid body. When fitting the lunar laser ranges Williams et al. detected four dissipation terms and computations of the lunar rotation including only tidal solid-body dissipation was not able to account for all four amplitudes, whereas a model with combined dissipation from tides and a fluid core could. This argument that tides plus a fluid-core/solid-mantle interaction satisfactorily explain the lunar rotational dissipation data, is the main point put forward by Williams et al. in arguing for a present-day molten lunar core. This contrasts with what has been done here where the implications of the solution parameters pertaining to lunar geophysics (notably k_2) as estimated by Williams et al. are explored in a quantitative manner. Accordingly, one might argue that since the two studies use different data to arrive at their conclusions, a molten core is now better accounted for.

[56] Concerning the Q-value used here, we take it as referring entirely to dissipation within the solid body and not core mantle boundary (CMB) fluid effects, since what has been measured is the effect of whole-body k_2/Q on mantle rotation. Furthermore, as the moment of inertia of the fluid core is $\sim 10^{-4}$ of the total, large changes in the core distortion or rotation would be needed to change the rotation of the mantle by a small amount reinforcing the assumption that almost all of the detected whole-body Q stems from the mantle. As concerns the separate LLR CMB interpretation, it should be noted that the low S wave speeds in the central layer are compatible with a liquid core or an extended partial melt. The inference of a fluid core from the LLR dissipation data [*Williams et al.*, 2001, 2004] is only compatible with an independently moving fluid core. That interpretation invokes dissipation from the motion of fluid with respect to the solid mantle at the core-mantle interface. To be compatible with this interpretation, a core made entirely of a partial melt would have to be extensively melted at the interface so that it behaved like a fluid.

[57] How does the size of our inferred core compare with that estimated by Williams et al.? Certain assumptions go into their calculation and in order to estimate the size of the core, they used turbulent boundary layer theory, as LLR is able to determine a coupling parameter between the fluid-core/solid-mantle interface. The coupling parameter, however, depends on radius, density and viscosity of the fluid core and these are not measured separately as discussed by Williams et al. Using the approximate boundary layer theory by *Yoder* [1995], they find maximum radii of 352 km for a liquid Fe core (ρ = 7.0 g/cm^3) and 374 km (both estimates are 1-σ upper limits) for a liquid Fe-FeS eutectic (ρ = 5.3 g/cm^3). These values are found to be in line with those estimated here, especially if the uncertainties on the unknown parameters going into the fluid dynamical calculations are taken into consideration, which as comprehensively discussed by Williams et al. can act to reduce core size such as when core/mantle topography is present. It might also be remarked that Williams et al., in their discussion of the core, note that liquid-outer/solid-inner core models are distinct possibilities as a completely solid

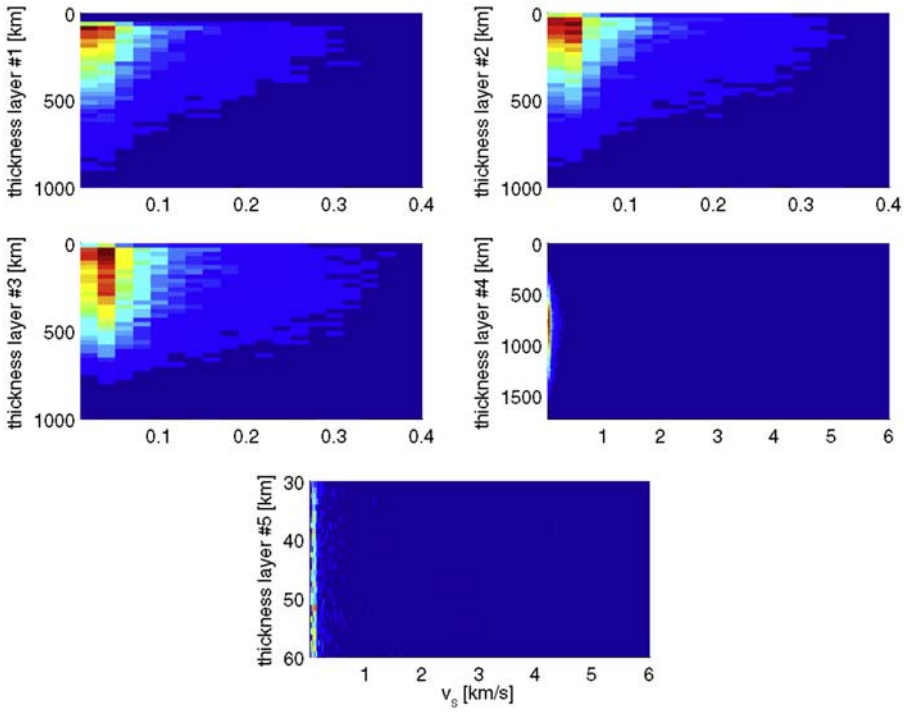

Figure 10. Two-dimensional conditional prior probability distribution showing the correlation that exists between the parameters v_s and d (thickness) for each individual layer. Layer #1 corresponds to the core, and layer #5 corresponds to the crust. Color coding follows Figure 7.

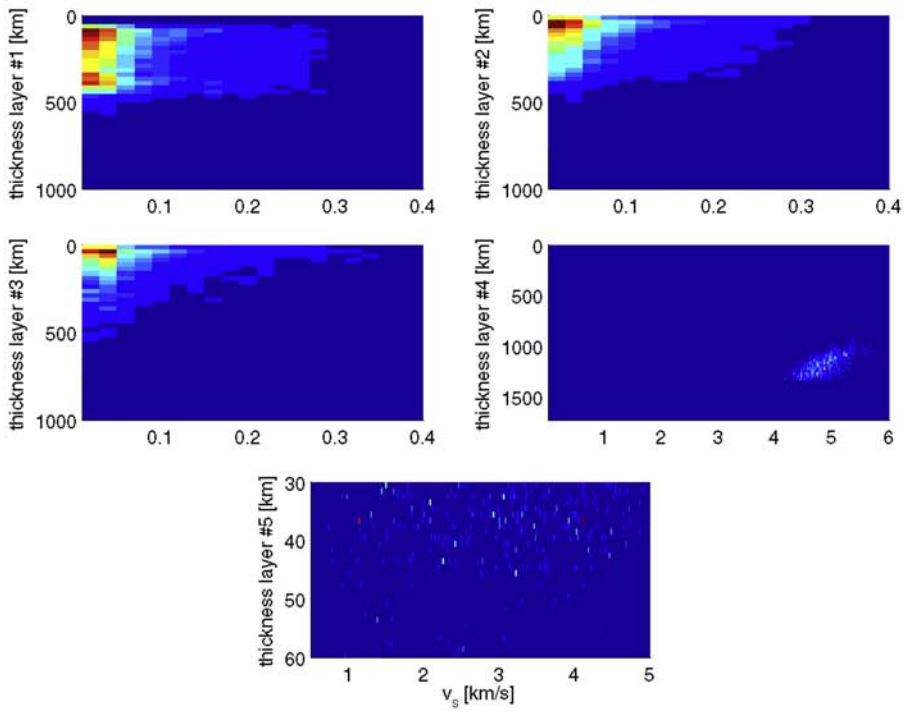

Figure 11. Two-dimensional conditional posterior probability distribution showing the correlation that exists between the parameters v_s and d (thickness) for each individual layer. Layer #1 corresponds to the core, and layer #5 corresponds to the crust. Color coding as in Figure 7. When comparing to prior information (Figure 10), the posterior distribution concerning the core has narrowed, although not as significantly as in Figure 8. However, a solution at $r \sim 350$ km and v_s close to 0 km/s is indicated by the posterior.

core is presently not realizable, given that there must be at least a thin fluid shell to apply the torque that LLR analyses detect. While our hypotheses are concerned with end-member models and we therefore in a strict sense do not consider the possibility of liquid-outer/solid-inner cores in this study, it is nonetheless interesting to note that some models satisfying $\mathcal{H}_2$ could be interpreted as implying this scenario. Figures 17 and 18 display 2-D prior and posterior conditional *pd*'s for the correlation between the parameters d and v_s. The results can be interpreted as indicating a solid core with a radius of around 380 km with a liquid layer, about 100 km thick, surrounding the core.

[58] Inferring the existence of a lunar core on the basis of the seismic data have been inconclusive, although *Nakamura et al.* [1974] reported a far-side meteorite impact, which showed a large delay of the *P* wave received at one of the stations, relative to the other three. The event time and location were estimated from arrivals at the three closest stations so that the arrival time at the fourth station could be predicted. The estimated location was nearly antipodal to the fourth station and the observed arrival time was delayed by about 50 s. Compressional wave velocity limits for the core were placed at 3.7–5.1 km/s, suggesting a low-velocity metallic composition. However, as pointed out by *Sellers* [1992], other interpretations of this far-side meteoroid impact are also possible, including ones that do not invoke the presence of a low-velocity core.

[59] From the curious scarcity of farside deep moonquakes, it can be argued, albeit only indirectly, that the state of the core is molten. The last comprehensive analysis in the Apollo era conducted by *Nakamura* [1983] found only a single farside deep moonquake (termed A_{33}), lying just over the eastern limb. There is no apparent reason as to why these should not exist, besides the fact that we can not observe them. Of the more than 12000 events that were registered by the seismic array slightly more than 7000 have until recently remained unclassified [*Nakamura*, 2003] and the consensus was that the latter group of events contained farside moonquakes. From the waveforms of the lone farside deep moonquake (A_{33}) a partial melt had been inferred earlier [*Nakamura et al.*, 1973]. It had been suggested that the presence of partial melt would attenuate *S* waves from farside moonquakes to such a degree that upon arrival at the seismic stations these were no longer visible, effectively leaving investigators no trace of the prominent shear wave arrival which is the tell-tale sign of a deep moonquake. The presence of a liquid core therefore easily explains why no true farside deep moonquakes (located on the farside, diametrically opposite the Apollo station array) have been observed until now, since shear waves emanating from them would be effectively damped when traversing the molten core. For the sake of completeness, let us mention that a recent promising approach involving the Apollo lunar seismic data is centered on the search for farside deep moonquakes [*Nakamura*, 2003]. Given the much enhanced computer capabilities of today the unclassified events have been reanalyzed by correlating events, as opposed to the art of visual correlation performed in the Apollo-era, to find matching signals, another tell-tale sign of deep moonquakes. As a result of this current investigation, new events as well as events belonging to the established hypocenters have been found, decreasing the number of unclassified events by 4000. Of some of the new events, waveforms have been found to be like those from A_{33}, with no clear shear wave arrivals at some of the stations, raising hopes that these are indeed farside deep moonquakes. A tentative localization of the new events has found that at least one and maybe two more are located on the far side [*Nakamura*, 2004].

[60] Of related interest is the suggested existence of partial melt in the lower mantle of the Moon. Two unrelated geophysical observations have been taken as indicating its existence. As already noted, *Nakamura et al.* [1973] were the first to suggest the probable presence of partial melt in the Moon, given that the lone far-side focus (A_{33}) was found to be a strong source producing large *P* and *S* wave arrivals at the closest stations (15 and 16), with bottoming depths for these rays at about 1100 km; the rays arriving at station 14 were found to bottom at 1200 km depth and are anomalous. While a strong *P* arrival is observed, there is no evidence for a shear wave arrival. At station 12, which is even more distant from A_{33}, a very small amount of energy is seen. Although model dependent, *S* waves are observed not to penetrate below a depth of about 1100 km, thereby suggesting a partially molten lunar mantle below this depth. A partially molten zone might plausibly dominate tidal damping as argued by Williams et al. and could account for the monthly tidal Q-value of 33 which is surprisingly low by terrestrial standards (tidal Q for the Earth is 370 [*Ray et al.*, 2002] whereas it is 92 ± 11 for Mars [*Yoder et al.*, 2003]). However, such a zone could not be localized by the LLR measurements. These observations are not unrelated given the fact that just above this zone lies the deep moonquake source region, which appears to be concentrated in the depth range 850–1000 km, with what seems to be an apparently rather sharp lower boundary [*Khan et al.*, 2000], indicating rheological changes in the deep lunar interior.

[61] In having to interpret our results in terms of mineralogical or compositional implications of the core we shall use the densities as stated by *Kuskov et al.* [2002]. They adopt the following values for a solid/liquid core of constant density based in part on measurements by *Sanloup et al.* [2000]: 8.1 g/cm^3 (γ-Fe), 5.7 g/cm^3 (Fe-10 wt%S) at 5 GPa and 1500°C; 5.15 g/cm^3 (eutectic Fe-FeS) and 4.7 g/cm^3 (troilite, FeS). How do these values compare with our results? The obvious interpretation of our results is of course that of liquid Fe core with a radius of ∼350 km. Other possibilities were also found possible, which included a core with a radius of around 400 km and a density of ∼6 g/cm^3, which is most easily interpreted as an Fe core containing some light alloying element, such as Si, S or C.

[62] How do our results compare with what has been obtained earlier? Concerning the lunar core, several lines of evidence, such as the moment of inertia [*Konopliv et al.*, 1998; *Lognonné et al.*, 2003], the induced magnetic dipole moment [*Hood et al.*, 1999], depletion of highly siderophile elements in the mare basalt source region [*Righter*, 2002] and the existence of remanent magnetism in lunar rocks [e.g., *Hood*, 1995] have independently hinted at its existence and it is the consensus that the Moon contains a small pure Fe or Fe-S alloy core (<450 km in radius, making up 1–4% of lunar mass). However, none of the data by themselves purporting to its existence, nor in combination, lead to an unequivocal estimate of its size nor its density

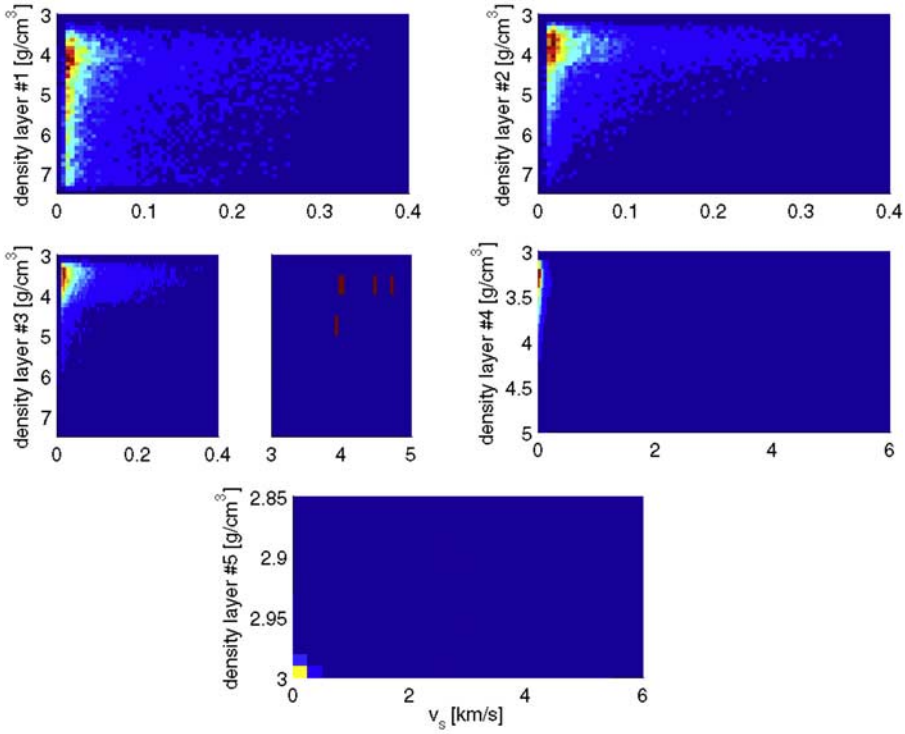

Figure 12. Two-dimensional conditional prior probability distribution showing the correlation that exists between the parameters v_s and ρ for each individual layer. Layer #1 corresponds to the core, and layer #5 corresponds to the crust. Color coding as in Figure 7.

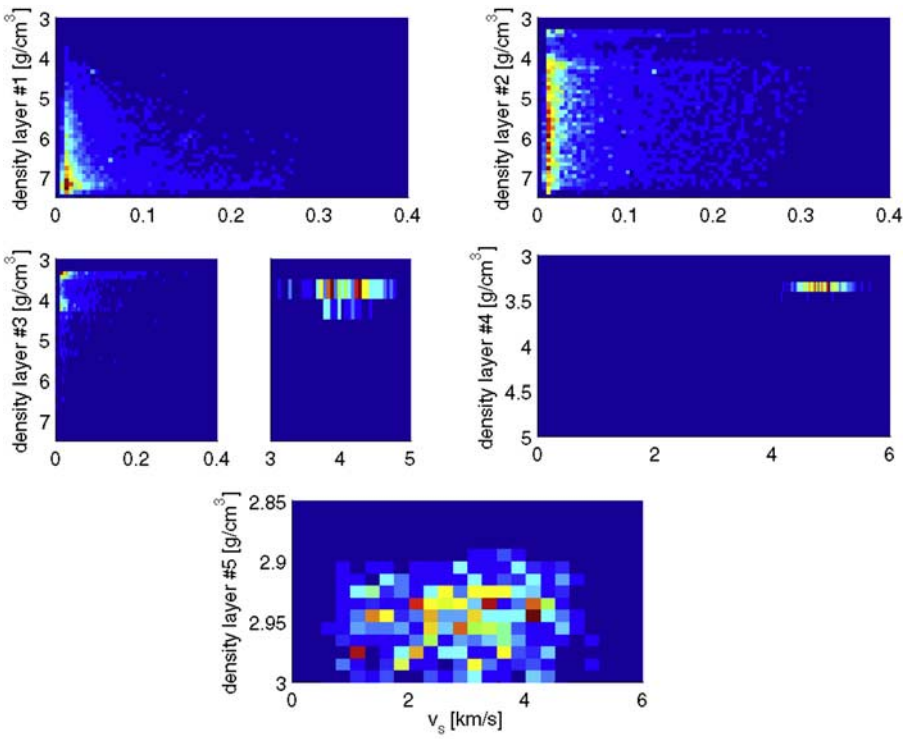

Figure 13. Two-dimensional conditional posterior probability distribution showing the correlation that exists between the parameters v_s and ρ for each individual layer. Layer #1 corresponds to the core, and layer #5 corresponds to the crust. Color coding as in Figure 7. Upon comparing to prior information concerning the core a significant change of the probability distribution is visible, indicating a solution with a large probability at $\rho \sim 7.2$ g/cm^3 and v_s close to 0 km/s.

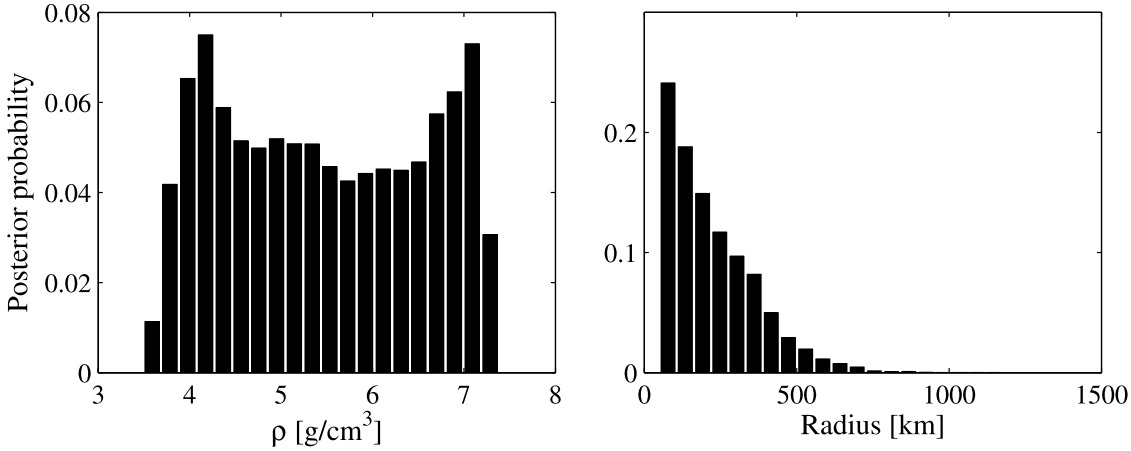

Figure 14. One-dimensional marginal posterior histograms for sampled values of core density and radius, from the inversion of only mass M and moment of inertia I. Comparing it to Figure 6 leaves little doubt that the lunar Love number k_2 is sensitive to the core.

[e.g., *Wieczorek and Zuber*, 2002]. Accordingly, other scenarios have been proposed, including one where the Moon's core is made of ilmenite [*Hess and Parmentier*, 1995].

[63] While thermal history models of the Moon are inherently nonunique given the very few constraints that bear directly on these, thermal considerations can provide some general information on the core. Since the melting

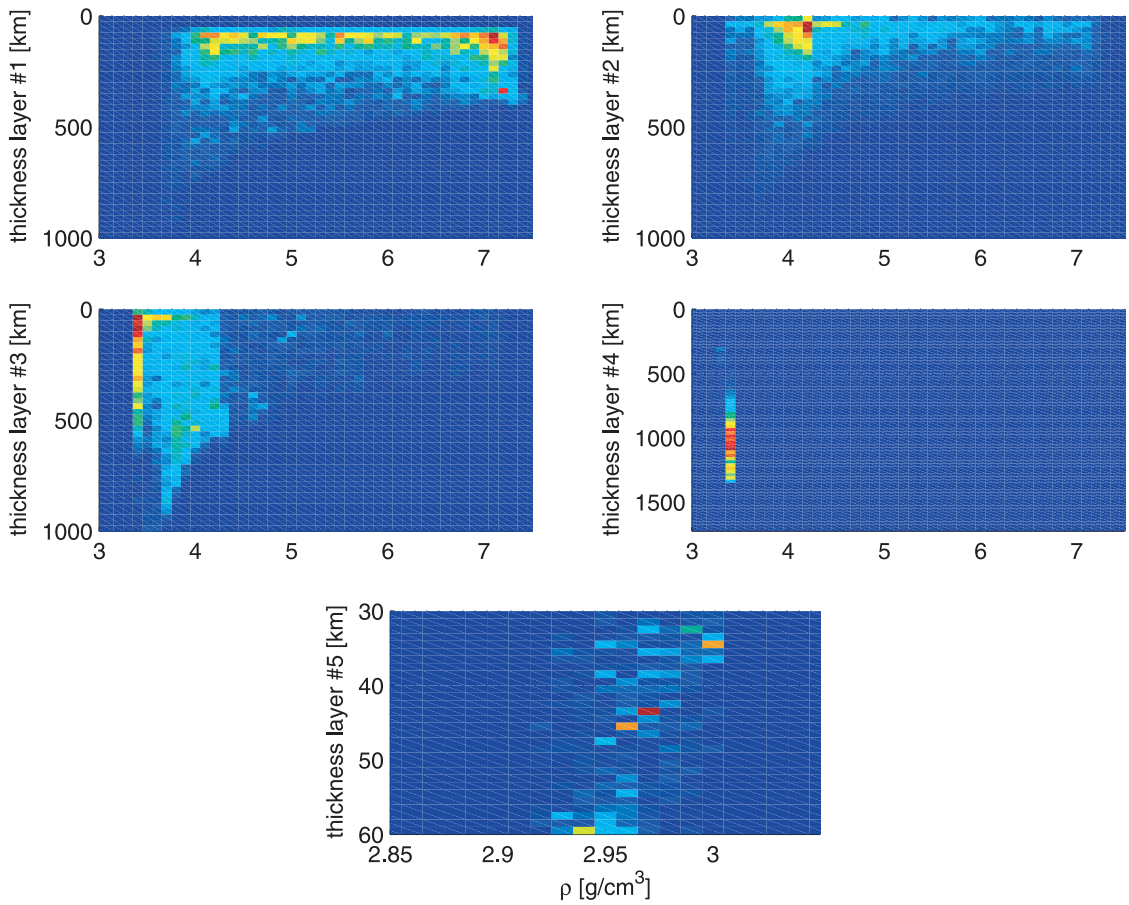

Figure 15. Two-dimensional conditional posterior probability distribution showing the correlation that exists between the parameters ρ and d (thickness) for each individual layer, obtained from the inversion of only M and I. As before, layer #1 corresponds to the core, and layer #5 corresponds to the crust. Color coding as in Figure 7. When compared to Figure 8 depicting the full posterior (inversion of k_2, Q, M and I), we see that for the core the distributions are different, which, like Figure 14, indicates that the lunar Love number k_2 is sensitive to the core structure.

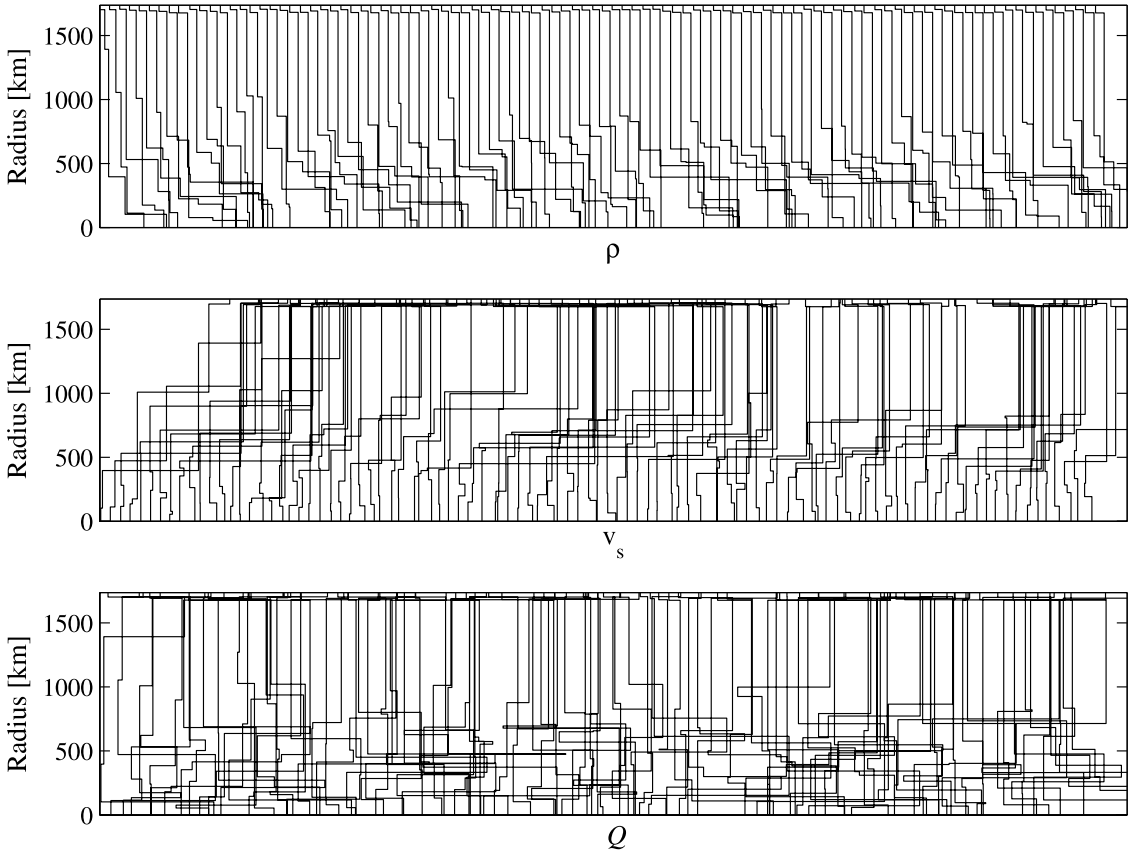

Figure 16. One hundred samples taken from the posterior probability distribution, obtained by inverting M and I. As in Figures 1 to 4, we are not plotting the logarithm of the individual parameters and so do not obtain homogeneous distributions, but ones that are skewed. The models plotted here all contain liquid low-velocity cores ($v_s \leq 0.5$ km/s) as prescribed by $\mathcal{H}_1$. Same horizontal separation as in Figures 1 to 4. Obvious differences between this posterior distribution and the full one (Figure 3) are present. While an inversion of only M and I does not provide any information on v_s and Q, we have nonetheless included the latter two here, to highlight this aspect, which is obvious when the v_s and Q profiles shown here are compared to prior information (Figure 1).

point of pure Fe is about 1600°C, a core made of pure Fe would presently have crystallized, given that present-day temperatures in the center of the Moon are currently estimated to be around 1400°C [*Spohn et al.*, 2000]. In the thermal modeling of, e.g., *Toksöz et al.* [1978], present-day central temperatures of ∼1450°C are achieved and it is stated by Toksöz et al. that if the Moon contains a small Fe-FeS core it is completely molten. The molten state of the core can thus be explained by including alloying elements such as S and/or C. This would act to lower the melting temperature to as much as 950°C [*Fei et al.*, 1997] for the eutectic composition, which of course is more in agreement with our second solution, briefly noted upon in the results section, indicating a core with a density of ∼6 g/cm^3 and a radius of ∼400 km.

[64] A number of studies concerned with the interpretation of the Nakamura seismic velocity model [*Nakamura*, 1983] in terms of chemical composition all led to the conclusion that a central core with a density different from that of the mantle was most probably needed to account for the geophysical data, i.e., the seismic velocities, mass and moment of inertia [e.g., *Hood and Jones*, 1987; *Mueller et al.*, 1988; *Kuskov et al.*, 2002]. Core sizes were found to range from 350 km (pure Fe core) to 530 km (troilite core) [*Kuskov et al.*, 2002].

[65] As reviewed by, e.g., *Hood* [1986] and *Hood and Zuber* [2000], electromagnetic sounding of the Moon by a single magnetometer in low-altitude orbit presents an alternative approach to obtain information on the existence and size of a metallic core. Exposure of the Moon for a prolonged period to an almost spatially uniform magnetic field in a near-vacuum environment, as happens monthly when the Moon passes through the lobe of the geomagnetic tail, induces electrical currents in the lunar interior. The resultant induced magnetic dipole moment is oriented opposite to the external field and what is measured in orbit is a small perturbation given by the sum of the steady and induced fields. The field will diffuse through the mantle (decaying after ∼5 hours or less) and induce currents near the surface of a possibly highly electrically conducting core which produces the negatively induced dipole moment. The amplitude of the residual induced moment can then be related to the core radius. While being able to provide bounds on the size of the core, the method is less sensitive to its composition. Using data from the Apollo 15 and 16 subsatellite magnetometers, *Russell et al.* [1981],

assuming that all measured effects were due to a metallic core, estimated its radius to be 439 ± 22 km. A recent independent attempt using the magnetometer onboard Lunar Prospector, assuming the induced field to be caused entirely by electrical currents near the surface of a highly electrically conducting metallic core, obtained a core radius of 340 ± 90 km [*Hood et al.*, 1999].

[66] Unlike the Earth, the Moon does not presently possess a magnetic field of internal origin. As the returned Apollo 11 samples were examined, a stable natural remanent magnetism, evocative of an ancient magnetic field, was found in the rocks. This came as a surprise, since early measurements by Explorer satellites had revealed a vanishingly small global lunar magnetic field. The pattern that emerged from the work done on the returned samples, showed that the most strongly magnetized rocks have ages between 3.9 and 3.6 aeons [*Fuller and Cisowski*, 1987]. From this it was deduced, tentatively, that a strong lunar magnetic field came into existence shortly after Serenitatis time, at about 3.9 aeons [*Cisowski and Fuller*, 1986], and that it decreased from a maximum strength of ~100 μT at 3.9 aeons to ~1 μT at 3.2 aeons [*Runcorn*, 1983]. The most prominent proposals are impact generated fields and generation of the field due to internal motion in a fluid lunar core, in close analogy to the Earth. *Runcorn* [1983] uses the dependence of paleointensity on age, as is evidenced by the decreasing field strength from ~4.0 to ~3.2 aeons, to argue that the magnetizing field was of internal origin, because while locally generated fields would not have had a simple dependence of age, a decrease in the field with decreasing age would be expected for a dynamo driven by internal energy sources that diminished with time. The size of the core needed to generate a dipole moment about 100 times smaller than the terrestrial dynamo, i.e., to establish the stipulated field strength at the lunar surface at 3.9 aeons, has been estimated at 400 km [*Fuller and Cisowski*, 1987]. However, it has to be noted that the remanent magnetization found in younger rocks (~1.5 Gyr) is difficult to explain with this scenario as a lunar dynamo is not thought to have operated at this late stage and is thus more easily explained within the context of impact processes [*Hood and Vickery*, 1984].

[67] How does the presence of a metallic core fit with the prevailing theory of lunar formation? As already mentioned in the introduction, it is the consensus view that the Moon formed as a result of a giant impact between the proto-Earth and a Mars-sized impactor, although it has proven rather difficult to find impacts capable of producing a Moon, since much of the material placed in orbit about the Earth actually lies within the Roche limit and would therefore be tidally disrupted and accreted back to Earth [*Canup and Esposito*, 1996; *Ida et al.*, 1997]. Recent simulations of the collision have therefore placed emphasis on the search for conditions, such as total mass, impactor-proto-Earth mass ratios and total angular momentum, under which enough material could be placed into Earth's orbit and outside the Roche limit. These investigations have resulted in two sets of Moon-forming impact models, satisfying the above constraints. One involves an early impact, while the Earth was only half-formed and a mass ratio between impactor and proto-Earth of 3:9 [*Cameron*, 2000], whereas the other one involves a late impact with a mass ratio of 1:9 [*Canup and Asphaug*, 2001; *Canup*, 2004]. Not only does the latter impact involve a smaller object, rendering it a more likely event, it also does away with the problem inherent in the early-impact scenario of having to explain why only the Earth continued to grow accumulating large amounts of iron and volatile material and not the iron- and volatile-poor Moon. Whichever scenario, both make the Moon from mantle material of the impactor and both involve subjecting the material making up the Moon to high temperatures, under which a metallic core would separate instantaneously. However, it has to be noted that the giant impact model at present is not capable of precisely predicting the thermal state of the early Moon [*Pritchard and Stevenson*, 2000]. It has nonetheless become a reasonably established fact that a significant part of and maybe even all of the Moon, shortly after it accreted from the silicate debris splashed into geocentric orbit, must have been molten to account for the feldspathic nature of the highland crust which is thought to have crystallized from a global magma ocean [e.g., *Warren*, 1985]. There is less agreement on the depth of melting with values ranging from shallow (200 km) to whole-Moon involvement [*Taylor*, 1986]. Using geochemical considerations, *Taylor* [1987], for example, showed that at least half of the Moon must have been molten to account for the thick aluminous crust. Formation of a core from a molten magma ocean has been discussed by *Stevenson* [1990] and is expected to be important in planetesimals up to lunar size [*Rushmer et al.*, 2000]. Core formation in the Moon would additionally lead to the sequestering of siderophile elements in order of their metal-silicate partition coefficients from the mantle into the core. Chemical analyses of lunar meteorites and returned samples have shown that the siderophile elements are depleted in the lunar mantle [e.g., *Newsom*, 1984] and this has been taken as strong evidence for the presence of a lunar metallic core [*Righter*, 2002]. However, since the giant-impact simulations have shown that the Moon is made up of impactor mantle material and it is assumed that the Earth and impactor have formed cores prior to impact, with the impactor's core accreting to the Earth, it has been argued that the siderophile element abundance in the impactor's mantle might have been depleted prior to collision, lying somewhere between the lunar and present-day terrestrial values [*Newsom and Taylor*, 1989], effectively doing away with the need for a lunar metallic core. *Righter* [2002] on the other hand, using metal-silicate partitioning coefficients that have been carried out at higher pressures and temperatures than previously available, argues strongly for the presence of a metallic core in order to explain the observed siderophile element concentrations in lunar basalts. As already pointed out, recent analysis of lunar laser ranging data [*Williams et al.*, 2001] and the improved value of the moment of inertia obtained from Lunar Prospector [*Konopliv et al.*, 1998] as well as electromagnetic sounding data [*Hood et al.*, 1999] constrain the size of the lunar core to be small (1–3% by mass) in agreement with our result and with the outcome of giant-impact simulations which place little iron in the silicate debris later accreting to form the Moon, although it has to be noted that these studies at their most conservative only imply upper bounds on core sizes [*Hood and Zuber*, 2000]. With this in hindsight and given the results presented here implying a molten core with a most probable radius and

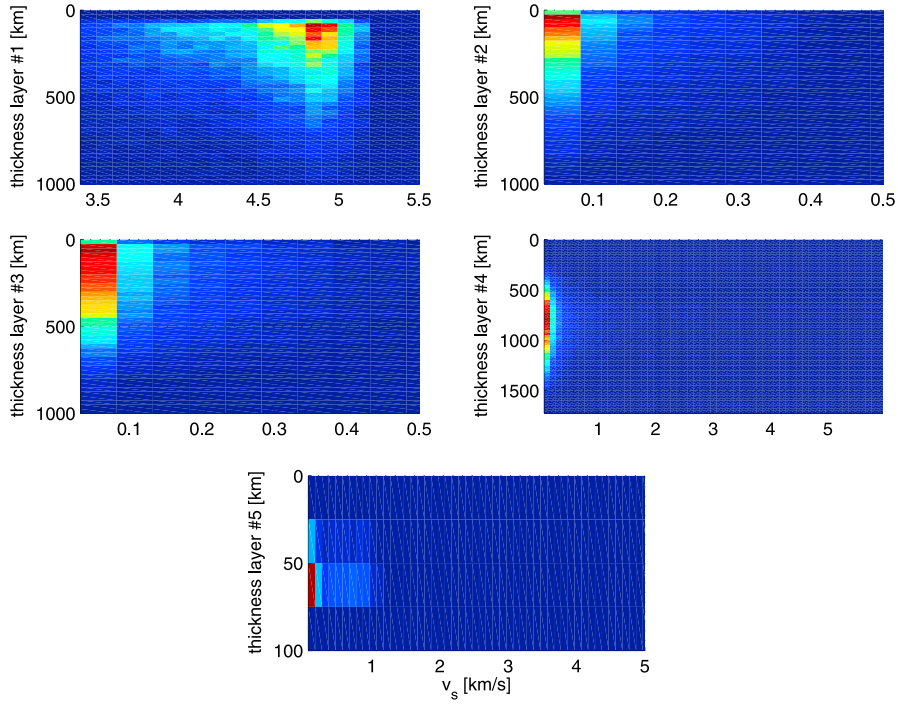

Figure 17. Two-dimensional conditional prior probability distribution for the models satisfying $\mathcal{H}_2$ depicting the correlation that exists between the parameters v_s and d (thickness) for each individual layer. Layer #1 corresponds to the core, and layer #5 corresponds to the crust. Color coding as in Figure 7.

density of ∼350 km and ∼7.2 g/cm^3, the existence of a small lunar metallic core is an almost inescapable conclusion.

[68] Finally, let us contemplate the fundamental question as to whether or not it is possible to infer information on the interior of the Moon or any other planet for that matter from four scalar numbers. From the point of view of the inverse problem it might reasonably well be considered underdetermined, however, this should by no means deter us, since underdetermined problems are the rule rather than the

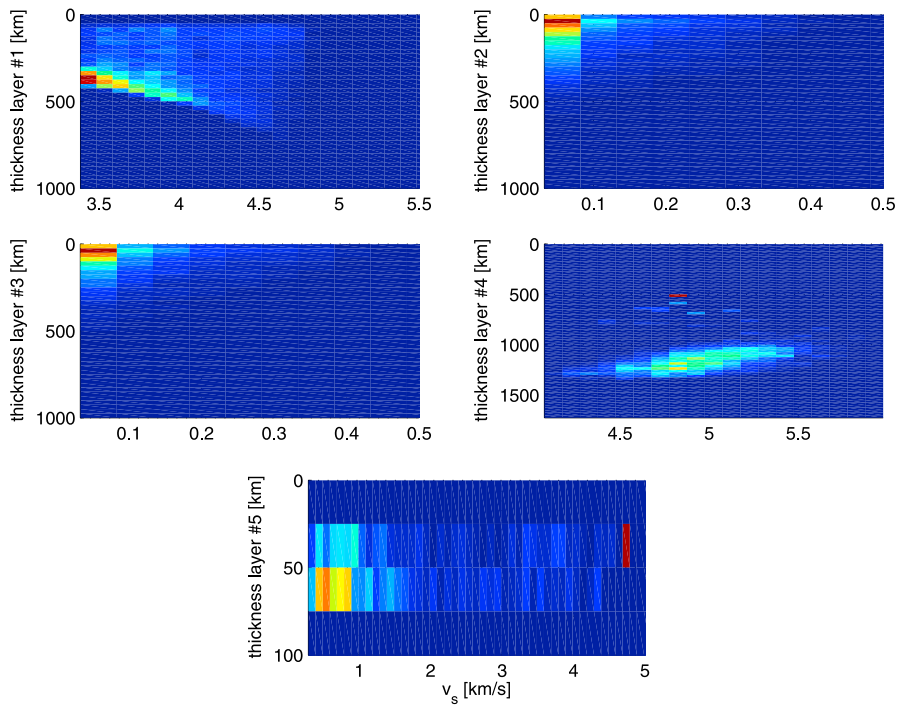

Figure 18. Two-dimensional conditional posterior probability distribution for the models satisfying $\mathcal{H}_2$ showing the correlation that exists between the parameters v_s and d (thickness) for each individual layer. Layer #1 corresponds to the core, and layer #5 corresponds to the crust. Color coding as in Figure 7.

exception especially within the domain of geophysical applications. Considering the numbers themselves, what sort of information is actually carried by these? - the mass or equally well the average density in itself is only able to place upper limits on the size of a core, while the moment of inertia tells us something about how much the density increases with depth. However, even when combining these two data there still remains a great many density models that will satisfy them [e.g., *Bills and Rubincam*, 1995]. The second degree tidal Love number, on the other hand, is known to be sensitive to the state and size of a core. Including Q provides additional constraints on the shear wave velocity structure. From the combination of these data, then, we would intuitively expect to be able to place certain constraints on the size of the core and in addition the Love number by itself ought in principle to be able to distinguish between a solid and a liquid core. A term such as 'in principle' is appropriate, because the final conclusions are of course dependent upon the uncertainties inherent in the data. Mars, which is believed to contain a substantial-sized core [e.g., *Yoder et al.*, 2003], thereby influencing k_2 to a much larger extent, than is the case for the Moon, is an obvious next candidate as is Mercury once data become available.

[69] **Acknowledgments.** We are grateful to Yosio Nakamura, Tim Van Hoolst, and Francis Nimmo for their thoughtful reviews. The manuscript also benefited from very stimulating discussions with Albert Tarantola. John Wahr is likewise thanked for comments. A. Khan acknowledges the financial support provided through the European Community's Improving Human Potential Programme under contract RTN2-2001-00414, MAGE. A portion of the research described in this paper was carried out at the Jet Propulsion Laboratory of the California Institute of Technology, under a contract with the National Aeronautics and Space Administration. This is IPGP contribution 1999.

References

Alterman, Z., H. Jarosch, and C. L. Pekeris (1959), Oscillations of the Earth, *Proc. R. Soc. London*, *Ser. A*, *252*, 80.

Anderson, J. D., R. A. Jacobson, E. L. Lau, W. B. Moore, and G. Schubert (2001), Io's gravity field and interior structure, *J. Geophys. Res.*, *106*, 32,963.

Bills, B. G., and D. P. Rubincam (1995), Constraints on density models from radial moments: Applications to Earth, Moon, and Mars, *J. Geophys. Res*, *100*, 26,305.

Bosch, M. (1999), Lithospheric tomography: From plural geophysical data to lithology estimation, *J. Geophys. Res.*, *104*, 749.

Brans, C., and R. H. Dicke (1961), Mach's principle and a relativistic theory of gravitation, *Phys. Rev.*, *124*, 925.

Bullen, K. (1963), *An Introduction to the Theory of Seismology*, 3rd. ed., 381 pp., Cambridge Univ. Press, New York.

Cameron, A. G. W. (2000), Higher resolution simulations of the giant impact, in *Origin of the Earth and Moon*, edited by R. M. Canup and K. Righter, p. 133, Univ. of Ariz. Press, Tucson.

Canup, R. M. (2004), Simulations of a late lunar forming impact, *Icarus*, *168*, 433.

Canup, R. M., and E. Asphaug (2001), Origin of the Moon in a giant impact near the end of the Earth's formation, *Nature*, *412*, 708.

Canup, R. M., and L. W. Esposito (1996), Accretion of the Moon from an impact-generated disk, *Icarus*, *119*, 427.

Castillo, J., N. Rappaport, A. Mocquet, and C. Sotin (2002), Clues on Titan's internal structure from Cassini-Huygens Mission, *Lunar Planet. Sci.*, *XXXIII*, abstract 1989.

Cisowski, S. M., and M. Fuller (1986), Lunar paleointensities via the IRMs normalisation method and the early magnetic history of the Moon, in *Origin of the Moon*, edited by W. K. Hartmann, R. J. Phillips, and G. J. Taylor, p. 411, Lunar and Planet. Inst., Houston, Tex.

Dahlen, F. A. (1972), Elastic dislocation theory for a self-gravitating elastic configuration with an initial static stress field, *Geophys. J. R. Astron. Soc.*, *28*, 357.

Dickey, J. O., et al. (1994), Lunar laser ranging: A continuing legacy of the Apollo Program, *Science*, *265*, 482.

Fei, Y., C. M. Bertka, and L. W. Finger (1997), High-pressure iron-sulfur compound, Fe_3S_2, and melting relations in the Fe-FeS system, *Science*, *275*, 1681.

Feldman, W. C., B. L. Barraclough, S. Maurice, R. C. Elphic, D. J. Lawrence, D. R. Thomsen, and A. B. Binder (1998), Major compositional units of the Moon: Lunar Prospector thermal and fast neutrons, *Science*, *281*, 1489.

Fuller, M., and S. M. Cisowski (1987), Lunar paleomagnetism, in *Geomagnetism*, vol. 2, edited by J. Jacobs, p. 304, Academic, San Diego, Calif.

Goins, N., A. Dainty, and M. N. Toksöz (1981), Lunar seismology: The internal structure of the Moon, *J. Geophys. Res.*, *86*, 5061.

Goldreich, P. (1967), Precession of the Moon's core, *J. Geophys. Res.*, *72*, 3135.

Good, I. (1988), The interface between statistics and philosophy of science, *Stat. Sci.*, *3*, 386.

Halliday, A. N., D.-C. Lee, and S. B. Jacobsen (2000), Tungsten isotopes, the timing of metal-silicate fractionation and the origin of the Earth and Moon, in *Origin of the Earth and Moon*, edited by R. M. Canup and K. Righter, p. 45, Univ. of Ariz. Press, Tucson.

Hess, P. C., and E. M. Parmentier (1995), A model for the thermal and chemical evolution of the Moon's interior: Implications for the onset of mare volcanism, *Earth Planet. Sci. Lett.*, *134*, 501.

Hood, L. L. (1986), Geophysical constraints on the lunar interior, in *Origin of the Moon*, edited by W. K. Hartmann, R. J. Phillips, and G. J. Taylor, p. 361, Lunar and Planet. Inst., Houston, Tex.

Hood, L. L. (1995), Frozen fields, *Earth Moon Planets*, *67*, 131.

Hood, L. L., and J. H. Jones (1987), Geophysical constraints on lunar bulk composition and structure: A reassessment, *J. Geophys. Res.*, *92*, 396.

Hood, L. L., and A. Vickery (1984), Magnetic field amplifications and generation in hypervelocity meteoroid impacts with application to lunar paleomagnetism, *Proc. Lunar Planet. Sci. Conf. 15th*, Part 1, *J. Geophys. Res.*, *89*, suppl., C211.

Hood, L. L., and M. T. Zuber (2000), Recent refinements in geophysical constraints on lunar origin and evolution, in *Origin of the Earth and Moon*, edited by R. M. Canup and K. Righter, p. 397, Univ. of Ariz. Press, Tucson.

Hood, L. L., D. L. Mitchell, R. P. Lin, M. H. Acuna, and A. B. Binder (1999), Initial measurements of the lunar-induced magnetic dipole moment using Lunar Prospector magnetometer data, *Geophys. Res. Lett.*, *26*, 2327.

Ida, S., R. M. Canup, and G. R. Stewart (1997), Lunar formation from an impact-generated disk, *Nature*, *389*, 353.

Jaynes, E. T. (1985), Where do we go from here?, in *Maximum Entropy and Bayesian Methods in Inverse Problems*, edited by C. R. Smith and W. T. Grandy Jr., p. 29, D. Reidel, Norwell, Mass.

Kaipio, J. P., V. Kohlemainen, E. Somersalo, and M. Vauhkonen (2000), Statistical inversion and Monte Carlo sampling methods in electrical impedance tomography, *Inverse Problems*, *16*, 1083.

Khan, A., and K. Mosegaard (2001), New information on the deep lunar interior from an inversion of lunar free oscillation periods, *Geophys. Res. Lett.*, *28*, 1791.

Khan, A., and K. Mosegaard (2002), An inquiry into the lunar interior: A nonlinear inversion of the Apollo lunar seismic data, *J. Geophys. Res.*, *107*(E6), 5036, doi:10.1029/2001JE001658.

Khan, A., K. Mosegaard, and K. L. Rasmussen (2000), A new seismic velocity model for the Moon from a Monte Carlo inversion of the Apollo lunar seismic data, *Geophys. Res. Lett.*, *27*, 1591.

Konopliv, A., A. B. Binder, L. L. Hood, A. B. Kucinskas, W. L. Sjögren, and J. G. Williams (1998), Improved gravity field of the Moon from Lunar Prospector, *Science*, *281*, 1476.

Kuskov, O. L., V. A. Kronrod, and L. L. Hood (2002), Geochemical constraints on the seismic properties of the lunar mantle, *Phys. Earth Planet. Inter.*, *134*, 175.

Lambeck, K. (1988), *Geophysical Geodesy: The Slow Deformation of the Earth*, 710 pp., Clarendon, Oxford.

Lawrence, D. J., W. C. Feldman, B. L. Barraclough, A. B. Binder, R. C. Elphic, S. Maurice, and D. R. Thomsen (1998), Global elemental maps of the Moon: The Lunar Prospector Gamma-Ray Spectrometer, *Science*, *281*, 1484.

Lognonné, P., and B. Mosser (1993), Planetary seismology, *Surv. Geophys*, *14*, 239.

Lognonné, P., J. Gagnepain-Beyneix, and H. Chenet (2003), A new seismic model of the Moon: Implications for structure, thermal evolution and formation of the Moon, *Earth Planet. Sci. Lett.*, *211*, 27.

Melchior, P. (1978), *The Tides of the Planet Earth*, 609 pp., Pergamon, New York.

Mosegaard, K. (1998), Resolution analysis of general inverse problems through inverse Monte Carlo sampling, *Inverse Problems*, *14*, 405.

Mosegaard, K., and M. Sambridge (2002), Monte Carlo analysis of inverse problems, *Inverse Problems*, *18*, R29.

Mosegaard, K., and A. Tarantola (1995), Monte Carlo sampling of solutions to inverse problems, *J. Geophys. Res.*, *100*, 12,431.

Mosegaard, K., and A. Tarantola (2002), Probabilistic approach to inverse problems, in *International Handbook of Earthquake and Engineering Seismology*, p. 237, Academic, San Diego, Calif.

Mueller, S., G. J. Taylor, and R. J. Phillips (1988), Lunar composition: A geophysical and petrological synthesis, *J. Geophys. Res.*, *93*, 6338.

Nakamura, Y. (1983), Seismic velocity structure of the lunar mantle, *J. Geophys. Res.*, *88*, 677.

Nakamura, Y. (2003), New identification of deep moonquakes in the Apollo lunar seismic data, *Phys. Earth Planet. Inter.*, *139*, 197.

Nakamura, Y. (2004), More far-side deep moonquake nests discovered, *Lunar Planet. Sci.*, *XXXV*, abstract 1155.

Nakamura, Y., D. Lammlein, G. V. Latham, M. Ewing, J. Dorman, F. Press, and M. N. Toksöz (1973), New seismic data on the state of the deep lunar interior, *Science*, *181*, 49.

Nakamura, Y., G. V. Latham, D. Lammlein, M. Ewing, F. Duennebier, and J. Dorman (1974), Deep lunar interior inferred from recent seismic data, *Geophys. Res. Lett.*, *1*, 137.

Newsom, H. E. (1984), The lunar core and the origin of the Moon, *Eos Trans. AGU*, *65*, 369.

Newsom, H. E., and S. R. Taylor (1989), Geochemical implications of the formation of the Moon by a single giant impact, *Nature*, *338*, 29.

Pritchard, M. E., and D. J. Stevenson (2000), Thermal aspects of a lunar origin by giant impact, in *Origin of the Earth and Moon*, edited by R. M. Canup and K. Righter, p. 179, Univ. of Ariz. Press, Tucson.

Ray, R. D., R. J. Eanes, and B. F. Chao (2002), Detection of tidal dissipation in the solid Earth by satellite tracking and altimetry, *Nature*, *381*, 595.

Righter, K. (2002), Does the Moon have a metallic core? Constraints from giant-impact modelling and siderophile elements, *Icarus*, *158*, 1.

Runcorn, S. K. (1983), Lunar magnetism, polar displacements and primeval satellites in the Earth-Moon system, *Nature*, *304*, 589.

Rushmer, T., W. G. Minarik, and G. J. Taylor (2000), Physical processes of core formation, in *Origin of the Earth and Moon*, edited by R. M. Canup and K. Righter, Univ. of Ariz. Press, Tucson, p. 227.

Russell, C. T., P. J. Coleman Jr., and B. E. Goldstein (1981), Measurements of the lunar induced magnetic moment in the geomagnetic tail: Evidence for a lunar core, *Proc. Lunar Planet. Sci. Conf. 12th*, 831.

Sanloup, C., F. Guyot, P. Gillet, G. Fiquet, M. Mezouar, and I. Martinez (2000), Density measurements of liquid Fe-S alloys at high pressure, *Geophys. Res. Lett.*, *27*, 811.

Segatz, M., T. Spohn, M. N. Ross, and G. Schubert (1988), Tidal dissipation, surface heat flow, and figure of viscoelastic models of Io, *Icarus*, *75*, 187.

Sellers, P. (1992), Seismic evidence for a low-velocity lunar core, *J. Geophys. Res.*, *97*, 11,663.

Smith, D. E., M. T. Zuber, G. A. Neumann, and F. G. Lemoine (1997), Topography of the Moon from the Clementine LIDAR, *J. Geophys. Res.*, *102*, 1591.

Sohl, F., H. Hussmann, B. Schwentker, T. Spohn, and R. D. Lorenz (2003), Interior structure models and tidal Love numbers of Titan, *J. Geophys. Res.*, *108*(E12), 5130, doi:10.1029/2003JE002044.

Spohn, T., W. Konrad, D. Breuer, and R. Ziethe (2000), The longevity of lunar volcanism: Implications of thermal evolution calculations with 2D and 3D mantle convection models, *Icarus*, *149*, 54.

Spohn, T., F. Sohl, K. Wieczerkowski, and V. Conzelmann (2001), The interior structure of Mercury: What we know, what we expect from BepiColombo, *Planet. Space Sci.*, *49*, 1561.

Stevenson, D. J. (1990), Fluid dynamics of core formation, in *Origin of the Earth*, edited by H. E. Newsom and J. H. Jones, p. 231, Lunar and Planet. Inst., Houston, Tex.

Tarantola, A. (1987), *Inverse Problem Theory*, 613 pp., Elsevier Sci., New York.

Tarantola, A., and B. Valette (1982), Inverse problems: Quest for information, *J. Geophys.*, *50*, 159.

Taylor, S. R. (1982), *Planetary Science: A Lunar Perspective*, 481 pp., Lunar and Planet. Inst., Houston, Tex.

Taylor, S. R. (1986), The origin of the Moon: Geochemical considerations, in *Origin of the Moon*, edited by W. K. Hartmann, R. J. Phillips, and G. J. Taylor, p. 125, Lunar and Planet. Inst., Houston, Tex.

Taylor, S. R. (1987), The unique lunar composition and its bearing on the origin of the Moon, *Geochim. Cosmochim. Acta*, *51*, 1297, 1987.

Tierney, L. (1994), Markov chains for exploring posterior distributions, *Ann. Stat.*, *22*, 1702.

Toksöz, M. N., A. T. Hsui, and D. H. Johnston (1978), Thermal evolutions of the terrestrial planets, *Moon Planets*, *18*, 281.

Van Hoolst, T., and C. Jacobs (2003), Mercury's tides and interior structure, *J. Geophys. Res.*, *108*(E11), 5121, doi:10.1029/2003JE002126.

Van Hoolst, T., V. Dehant, F. Roosbeek, and P. Lognonné (2003), Tidally induced surface displacements, external potential variations and gravity variations on Mars, *Icarus*, *161*, 281.

Wahr, J. M., and Z. Bergen (1986), The effects of mantle anelasticity on nutations, Earth tides and tidal variations in rotation rate, *Geophys. J. R. Astron. Soc.*, *87*, 633.

Warren, P. H. (1985), The magma ocean concept and lunar evolution, *Annu. Rev. Earth Planet. Sci.*, *13*, 201.

Wieczorek, M. A., and M. T. Zuber (2002), The "core" of the Moon: Iron or titanium rich?, *Lunar Planet. Sci.*, *XXXIII*, abstract 1384.

Will, C. M. (1993), *Was Einstein Right?*, 279 pp., Oxford Univ. Press, New York.

Williams, J. G., D. H. Boggs, C. F. Yoder, J. T. Radcliff, and J. O. Dickey (2001), Lunar rotational dissipation in solid body and molten core, *J. Geophys. Res.*, *106*, 27,933.

Williams, J. G., D. H. Boggs, and J. T. Ratcliff (2004), Lunar core and tides, *Lunar Planet. Sci.*, *XXXV*, abstract 1398.

Wood, J. (1986), Moon over Mauna Loa: A review of hypotheses of formation of Earth's Moon, in *Origin of the Moon*, edited by W. K. Hartmann, R. J. Phillips, and G. J. Taylor, p. 12, Lunar and Planet. Inst., Houston, Tex.

Yoder, C. F. (1995), Venus' free obliquity, *Icarus*, *117*, 250.

Yoder, C. F., A. S. Konopliv, D. N. Yuan, E. M. Standish, and W. M. Folkner (2003), Fluid core size of Mars from detection of the solar tide, *Science*, *300*, 299.

Zschau, J. (1978), Tidal friction in the solid Earth: Loading tides versus body tides, in *Tidal Friction and the Earth's Rotation*, edited by P. Brosche and J. Sundermann, Springer-Verlag, New York.

A. Khan and P. Lognonné, Département de Géophysique Spatiale et Planétaire, Institut de Physique du Globe de Paris, 4 Avenue de Neptune, 94107 St. Maur Cedex, France. (khan@ipgp.jussieu.fr; lognonne@ipgp.jussieu.fr)

K. Mosegaard, Department of Geophysics, Niels Bohr Institute for Astronomy, Geophysics and Physics, University of Copenhagen, Juliane Maries Vej 30, 2100 Copenhagen Oe, Denmark. (klaus@gfy.ku.dk)

J. G. Williams, Jet Propulsion Laboratory, MS 238-332, 4800 Oak Grove Drive, Pasadena, CA 91109, USA. (james.g.williams@jpl.nasa.gov)